

Abstract

**Radiological
Technology**

SCHEDULE

Session 1 : 11 : 00 ~ 12 : 00

Session chair: Prof. Yoshie Kodera

1. Effect of reconstruction filter on image in dental cone beam computed tomography
Yuuki Houno
2. Characteristics of image in dual-energy computed tomography(CT) imaging
Dae Hong Kim
3. Verification of lateral biological dose distribution with microdosimetric kinetic model
in carbon-ion radiotherapy
Mikoto Tamura
4. The impact of secondary particles on in-beam PET imaging for dose verification in
carbon ion therapy
Su Jung An

Session 2 : 13 : 30 ~

Session chair: Prof. Hee Joung Kim

5. Evaluation of radiation dose to organs and tissues in infant X-ray CT
Takanori Ishii
6. Digital breast tomosynthesis and digital mammography- A comparison of figures of
merit for various average glandular doses
Ye Sle Kim
7. Reduction of patient dose in digital mammography: Simulation of low-dose image
from routine-dose
Yuki Saito

- 15 minutes rest -

Session chair: Prof. Haruo Isoda

8. Optimization of the angle between detector modules in a dual-head cardiac SPECT
Woo Jin Jo
9. Accuracy of 3D cine phase contrast MR flow measurement for common carotid
arteries
Ikki Tozawa
10. A high resolution SPECT system with a photon counting detector: Monte Carlo
simulation studies
Young Jin Lee

EFFECT OF RECONSTRUCTION FILTER ON IMAGE IN DENTAL CONE BEAM COMPUTED TOMOGRAPHY

Y. Houno¹⁾, T. Hishikawa²⁾, K. Goto³⁾, Y. Kodera¹⁾

1) Department of Radiological Sciences, Nagoya University Graduate School of Medicine, Nagoya, Japan

2) Department of Periodontology, School of Dentistry, Aichi Gakuin University, Nagoya, Japan

3) Department of Radiological Technology, Aichi Gakuin University Dental Hospital, Nagoya, Japan

Introduction

Recently, dentistry diagnoses have been performed using panoramic radiography or dental X-rays, but cone-beam CT (CBCT), which can obtain more information, has been gaining attention. CBCT has high spatial resolution, but it is difficult to describe that teeth and alveolar bones separately because the reconstructed image is blurred. It is important to know the condition of alveolar bones in diagnosis of periodontal disease or simulation of implant placement.

In CBCT, spatial resolution is influenced by machine characteristics such as detector spacing, focal spot size, and overall geometry. In addition, reconstruction parameters such as the voxel size and reconstruction filter influence the spatial resolution. However, users cannot change the machine characteristics. Thus, we examined the use of a reconstruction filter to provide a sharp image.

Materials and Methods

1. Exposure of phantom

We exposed a head, copper wire (0.28 mm diameter), and water phantoms with the Alphard “3030,” which is a cone-beam CT manufactured by Asahi Rentgen (Fig.1). The Alphard “3030” has four exposure modes for CT, and each mode has a different field of view [D-mode: 51 mm × 51 mm (voxel size: 0.1 mm); I-mode: 102 mm × 102 mm (voxel size: 0.2 mm); P-mode: 153 mm × 153 mm (voxel size: 0.3 mm); C-mode: 200 mm × 179 mm (voxel size: 0.39 mm)]. In this study, we selected the I-mode to obtain raw data and reconstructed two dimensional (2D) images.

We then created a three dimensional (3D) image from the reconstructed 2D images in INTAGE Realia, which is free software and a DICOM 3D viewer.

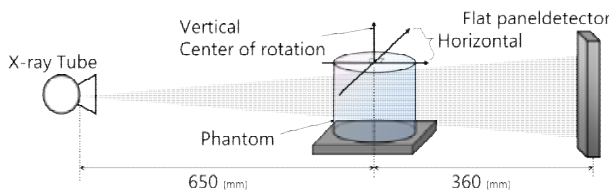


Fig.1 Experimental system

Table 1 Exposure conditions

Parameter	Value
Tube voltage	80 kV
Tube current	5 mA
Exposed time	17 sec
Focus - rotation center distance	650 mm
Source - image distance	1010 mm
Matrix of flat panel detector	768×768
Pixel pitch	0.39 mm
Focus size	0.6 mm
Number of view	510
Cone angle (Head side)	4.2 degree
Cone angle (Foot side)	5.9 degree

2. Reconstruction in OSCaR

First, we reconstructed the raw data with OSCaR[1] (open-source cone-beam reconstructor), which is a software package written in Matlab code and can be used to easily change a reconstruction filter. This software uses the FDK (Feldkamp) algorithm, which is one of the most widely referenced algorithms and a popular approximation for CBCT reconstruction. This algorithm is based on the filtered back-projection method.

We could not load OSCaR with the raw data at the original size, so we trimmed the image by imageJ and reconstructed it with a new reconstruction filter developed in this study. This filter is shown in Fig.2 as a New Filter.

We then created a 3D image, as mentioned in previous section.

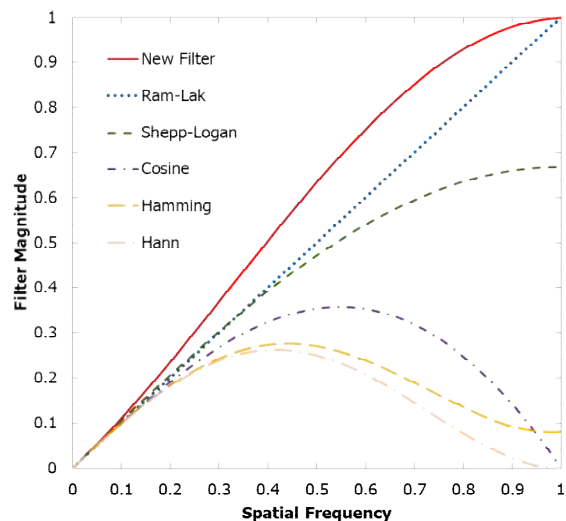


Fig.2 Reconstruction filter

3. Measurement of sharpness and granularity

For the wire and water phantom image, we calculated the modulation transfer function (MTF) and Wiener spectrum (WS)[2]. The MTF, which is calculated from the point spread function, is the established method for characterizing the spatial response of an image. In this study, we used a wire method (Fig.3). The WS is a valuable tool for assessing the noise power of an image in the spatial frequency domain and is a useful index. In this study, we calculated it by virtual slit method (Fig.4).

We calculated images reconstructed both by Alphard “3030” and by our method.

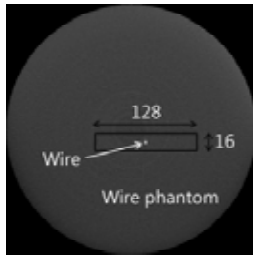


Fig.3 Wire method

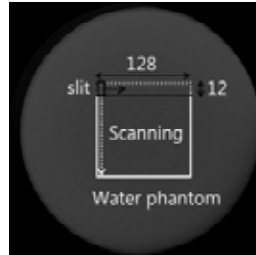


Fig.4 Virtual slit method

Results and Discussion

1. Comparison of 2D images

Figure 5a shows the image reconstructed by Alphard “3030,” and Fig.5b shows by our method. In 2D, the image reconstructed with our method clearly shows the pulp cavity and structure of alveolar bones, but it is slightly little noisy.

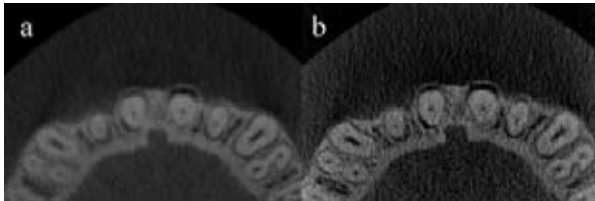


Fig. 5 Comparison of 2D images

2. Comparison of 3D images

Figure 6a shows the image reconstructed by Alphard “3030,” and Fig.6b shows by our method. In 3D, the image reconstructed with our method shows a gritty surface, but it can describe the area between the teeth.

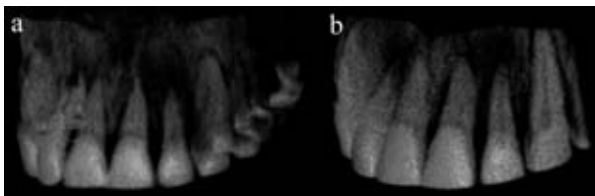


Fig. 6 Comparison of 3D images

3. Measurement of sharpness and granularity

The MTF and WS measurement results are shown in Figs.7 and 8. Our method improved the image sharpness but also increased the image noise. We thought that because we used a reconstruction filter which emphasized high frequency. These results fit with a comparison of the 2D/3D images.

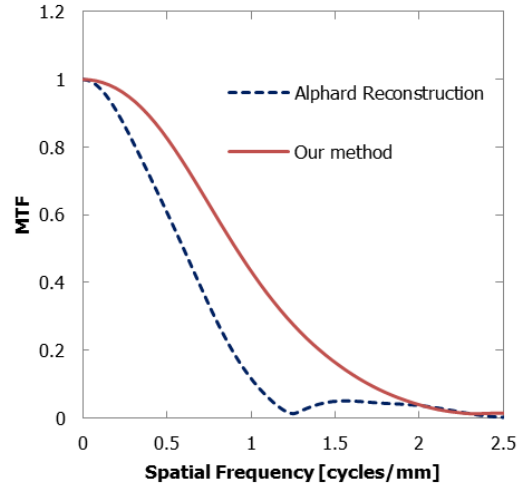


Fig.7 MTF

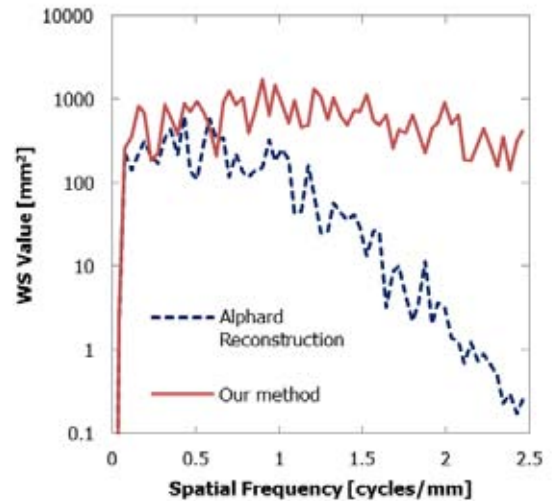


Fig.8 WS

Conclusions

We were able to obtain a sharp image in this study and determined that the reconstruction filter and the image sharpness and granularity are strongly related. However, a higher spatial resolution leads to an increased noise level.

In the future, we will develop a method that will maintain the sharpness and yet be noiseless. Furthermore, we will try to reduce metal artifacts and have our method evaluated by dentists.

References

- [1]Rezvani N, et al. (2010) An Open Source ConeBeam CT Reconstruction Tool for Imaging Research. American Association of Physicists in Medicine
- [2]Ichikawa K, Muramatsu Y. (2009) Measurement of X-ray CT image. Ohmsha: 29-118

Author address

E-Mail: houno.yuuki@f.mbox.nagoya-u.ac.jp

CHARACTERISTICS OF IMAGE IN DUAL-ENERGY COMPUTED TOMOGRAPHY(CT) IMAGING

D.H. Kim¹⁾, H. J. Kim¹⁾, C.L. Lee¹⁾, P.H. Jeon¹⁾, Y.J. Lee¹⁾, Y.S. Kim¹⁾

1) Department of Radiological Sciences, Yonsei University, Wonju, Korea

Introduction

Dual-energy computed tomography (DECT) is commonly used to obtain information such as tissue segmentation, plaque segmentation in angiography, and lung perfusion [1, 2]. As the dual-energy (DE) scan includes low- and high-energy images, the image quality and the dose dependence of the phantom size need to be compared to those in single-energy (SE) image. Furthermore, DE images must optimize the image quality within recommended dose limitations. Hence, The purpose of this study was to estimate the image quality of head and abdomen phantoms with SE and DE mixed methods. The results from SE and DE CT scans were compared under routine clinical exposure conditions. The scan protocols for tube current such as mA was alternated withing the recommended limited dose levels while the other scan protocols were fixed in SE and DE scans. The dose ranges were extended within the recommended dose levels for the head and the abdomen phantom.

Materials and Methods

Data Acquisition: The image quality and the radiation dose of SE and DE scans in linearly mixed method were evaluated for head and abdomen phantoms. The equation reported by Yu *et al.* for obtaining the leneraly-mixed image is as follows:

$$I = w_L I_L + w_H I_H$$

where I_L and I_H denote the low- and high-energy scan images, respectively, w_L and w_H are the weighting factors for the low- and high-energy scan images. $w_L + w_H = 1$. w_L is given by

$$w_L = \frac{C_L(\sigma_{H,s}^2 + \sigma_{H,b}^2)}{C_L(\sigma_{H,s}^2 + \sigma_{H,b}^2) + C_H(\sigma_{L,s}^2 + \sigma_{L,b}^2)}$$

where C_L and C_H are the contrasts between the signal and the noise for low- and high-energy cans, $\sigma_{L,s}$ and $\sigma_{L,b}$ are the noised expressed as standard deviations at the signal and the background images in low-energy scans, and $\sigma_{H,s}$ and $\sigma_{H,b}$ are the noises at the signal and the background in high-energy scans, respectively.

With head and abdomen phantom, we used x-ray tube voltages of 80 and 140 kV to obtain results similar to those of DE CT scans. The SE scans, typically 120 kV, for the head and the abdomen phantoms were performed with scan protocols based on the International Electrotechnical Commission (IEC).

CTDI_w: The $CTDI_w$ values of SE and DE scan were measured for head (16 cm diameters) and abdomen (32 cm diameter) Polymethylmethacrylate (PMMA) phantom. The $CTDI_w$ can be obtained from the $CTDI_{100}$. The $CTDI_{100}$ was measured using bothe head and abdomen phantoms with nine holes and a pencil ion chamber for the CT (Radical Corporation, 20X6-3CT, CA, USA). The values of $CTDI_{100}$ were calculated with the following equation:

$$CTDI_{100} = \frac{M \times Chamberlength(cm) \times F \times tp \times cf}{n \times T}$$

where M is the measured value in Roentgen, F is the exposure-to-dose conversion factor (0.78 cGy/R in acryl), tp is the correction factor for both temperature and pressure, cf is the chamber calibration factor, n is the number of slices, and T is the slice thickness (cm). The dose measurements

were estimated at the center and four peripheral locations (3 o'clock, 6 o'clock, 9 o'clock, 12 o'clock). The $CTDI_w$ can be obtained by using a weighted $CTDI_{100}$ from the center and prepheral locations and the following the equation:

$$CTDI_w = \frac{1}{3}CTDI_c + \frac{2}{3}CTDI_p$$

where $CTDI_c$ is the $CTDI_{100}$ measured in the center, and $CTDI_p$ is the mean of the $CTDI_{100}$ values measured at the 3 o'clock, 6 o'clock, 9 o'clock, and 12 o'clock positions.

Image Evaluation: We chose the image quality metric as the contrast-to-noise ratio (CNR) for the quantitative method for the head and the abdomen phantoms. The CNR is calculated as

$$CNR = \frac{|S_s - S_b|}{\sqrt{\sigma_s^2 + \sigma_b^2}}$$

where S_s and S_b are the signal intensities of the signal and background, respectively, and σ_s and σ_b are the noise values for the signal and background in Region of Interest (ROI).

Results

Estimation of CNR and CTDI_w in SE and DE scans: The CTDI_w was within European Commission (EC) recommendataion, 60 mGy for Head and 35 mGy for abdomen, respectively (Table 1).

Table 1 Diagnostic reference levels for CT examination of adults (European Commission, 1999)

Examination	Diagnostic reference level	
	CTDI _w (mGy)	DLP (mGy cm)
Head	60	1050
Abdomen	35	780

The maximum values of the CNR for SE and DE scans were 115.50 and 133.45 in similar dose regions for the head phantom, respectively in this work. The minimum values of CNR for SE and DE scans were 107.53 and 119.49, respectively. In the abdomen phantom anlysis, the maximum values of the CNR SE and DE scans were 41.83 and 54.58 in similar dose regions, respectively. The minimum values of the CNR values for SE and DE scans were 39.73 and 50.44, respectively.

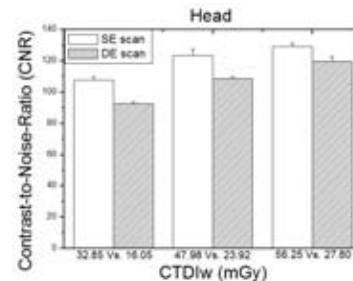


Figure 1. Comparisons of CNR values in head phantoms between single-energy (SE) and dual-energy (DE) scans at one-half the radiation dose of SE scans.

One-half of the doses for SE scans were chosen for DE scans to validate dose reduction, as described in Fig. 1 and 2. In the SE scans for the head phantom, the CNR values were 107.53, 123.58, and 129.26 at 32.85 mGy, 47.98 mGy, and 56.25 mGy, respectively. And the CNR values for the DE scans were 92.48, 108.70, and 119.49 at 16.05 mGy, 23.92 mGy, and 27.80 mGy, respectively. In the abdomen image evaluation, the

CNR values for the SE scans were 41.32, 41.78, 44.80, and 44.47 at 17.32 mGy, 20.65 mGy, 25.67 mGy, and 28.85 mGy, respectively. The CNR values for DE scans were 36.93, 42.83, 46.81, and 50.44 at 8.36 mGy, 10.48 mGy, 12.67 mGy, and 14.41 mGy, respectively.

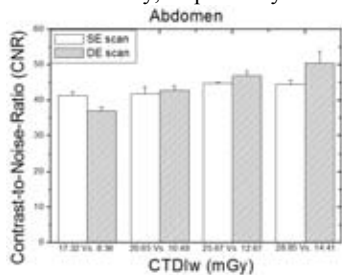


Figure 2. Comparisons of CNR values in abdomen phantoms between SE and DE scans at one-half the radiation dose of SE scans.

Figures 3 and 4 show the dose evaluations between SE and DE scans at similar CNRs. The doses between SE and DE scans were evaluated when the image qualities were similar. With the head phantom, the doses in the SE scans were 32.85, 38.70, and 54.19 mGy at CNR values of 107.53, 120.98, and 126.82, respectively. The doses in the DE scans were 23.92, 27.80, and 32.05 mGy at CNR values of 108.70, 119.49, and 127.42, respectively. For the abdomen phantom, the doses were 19.37, 29.39, and 31.94 mGy at CNR values of 41.83, 47.59, and 49.34 for SE scans, and the dose for DE scans were 10.48, 12.67, and 14.41 mGy at CNR values of 42.83, 46.81, and 50.44, respectively.

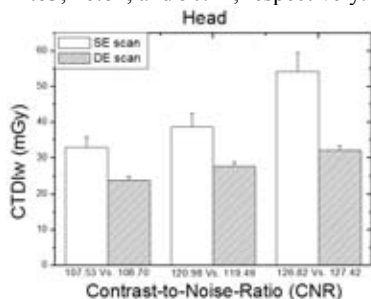


Figure 3. The dose evaluations at similar dose points for SE and DE scans in head phantom.

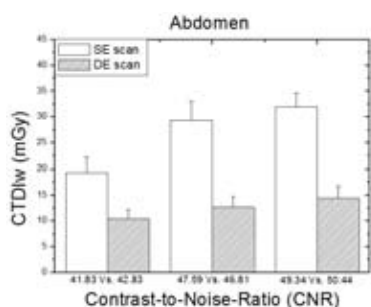


Figure 4. The dose estimations at similar dose regions for SE and DE scans in abdomen phantom.

Estimation of CNR and CTDIw in clinical radiation exposure conditions: In SE scans, the routine radiation exposure condition for the current on the head ranged from approximately 300 to 360 mAs at Yonsei University Wonju Christian Hospital. The CNR value was 126.82 for this range of currents for SE scans. The CNR of 127.42 in DE CT scans is comparable to the CNR value for the SE scans for head phantoms; the associated doses for SE and DE scans were 54.19 and 32.05 mGy, respectively. The current for the abdomen imaging ranged from 250 to 300 mAs. The CNR values for SE and DE scans within this range were 41.83 and

42.83, and the radiation doses were 19.37 and 10.48 mGy, respectively.

Discussion

In this study, CNR values heavily depended on the phantom size. The CNR values for the DE scans were higher than these for the SE scans for both head and abdomen phantoms in similar dose regions. The CNR improvement of DE images was remarkable, with maxima of 18.50 and 30.48 % for the head and the abdomen phantoms, respectively, relative to SE images. These results contributed to the dose reduction observed using DE CT.

When comparing the dose reduction effect, Figures 1 and 2 demonstrate that about one-half the dose could be used for the head and the abdomen regions when applying DE scans. The SE scan was outperformed in terms of CNR values for head phantoms at every dose comparison. The CNR values were 16.27, 13.69, and 8.18 % higher for head phantoms when using SE scans. The CNR results for the head phantom indicate that the dose reduction effect was approximately 50% for similar CNR values. The CNR difference between SE and DE scans decreased when the current was increased. Relative to the SE scan, the DE demonstrated higher CNR values than the SE scan, except for one point for the abdomen phantoms at one-half the dose. As a point of comparison between the 32.85 mGy (SE) and the 16.05 mGy (DE) scans, the CNR of the SE scan was 11.89% higher whereas the CNR values for DE scans were 2.45, 4.29, and 11.84% higher. For the abdomen study, the CNR values for SE scans using abdomen phantoms were 10.62 % higher than those of DE scans at 17.32 vs. 8.36 at one-half the radiation dose of the SE scans. With increasing radiation dose, the CNR values of the DE scan increased from 2.51% to 13.42%. Thus, a DE scan of the abdomen can be used with one-half of the radiation dose for a similar SE scan.

In Figures 3 and 4, the dose evaluations at similar CNR points are presented using SE and DE for head and abdomen phantoms. Greater dose increases were required for single energy CTs to obtain CNRs similar to the DE CTs for both head and abdomen phantoms. These results also included the dose reduction aspect of DE CT.

We estimated the image quality and dose between SE and DE scans in routine exposure conditions seen in clinical practice. Figures 3 and 4 show the evaluation for two scans in which the dose was reduced up to 40.86 and 45.90% for the head and the abdomen phantoms, respectively.

Conclusions

The current study suggests that DE scans can contribute to a reduced radiation dose while maintaining image quality by using the only current alternation. The DE scan achieved a higher CNR with one-half the radiation dose of a single-energy scan of the abdomen.

References

- [1]Bazalova M, Carrier JF, Beaulieu L, Verhaegen F. Tissue segmentation in Monte Carlo treatment planning: a simulation study using dual-energy CT images. *Radiother and Oncol.* 2008;86(1):93-98.
- [2]Boll DT, Merkle EM, Paulson EK, Mirza RA, Fleiter TR. Calcified vascular plaque specimens: assessment with cardiac dual-energy multidetector CT in anthropomorphically moving heart phantom. *Radiol.* 2008;249:119-126.

Author address

E-Mail: goldcollar011@yonsei.ac.kr

VERIFICATION OF LATERAL BIOLOGICAL DOSE DISTRIBUTION WITH MICRODOSIMETRIC KINETIC MODEL IN CARBON-ION RADIOTHERAPY

M.Tamura¹⁾, Y.Iwamoto¹⁾, T.Rachi¹⁾, K.Ota²⁾, A.Hemmi³⁾, T.Shimozato⁴⁾, Y.Obata⁵⁾, H.Oguchi¹⁾, M.Komori¹⁾

1) Department of Radiological Sciences, Graduate School of Medicine, Nagoya University, Nagoya, Japan

2) Okazaki City Hospital, Okazaki, Japan, 3) Komaki City Hospital, Komaki, Japan

4) Iwata City Hospital, Iwata, Japan, 5) Ichinomiya Municipal Hospital, Ichinomiya, Japan

Introduction

In a carbon-ion radiotherapy, it is essential to evaluate not only the absorbed dose but also the biological dose because relation between the survival curve and the dose changes drastically due to the kinetic energy of particles. The biological dose is defined as the absorbed dose multiplied by the relative biological effectiveness (RBE). The microdosimetric kinetic model (MKM) was useful for calculating the survival curves of human salivary gland (HSG) tumor cells in response to treatment with mono-energetic heavy-ion beams. The modified MKM which considered over-kill effect was shown to be calculate the RBE even mixed-beam radiation such as spread-out Bragg peak (SOBP) carbon-ion beam without particle identification by Y. Kase et al. [1][2]. The biological depth dose distribution calculated by the modified MKM has been known well, however, there are not sufficient reports about the lateral biological dose distribution. Furthermore, the lateral RBE distributions were regarded as constant in the carbon-ion treatment planning system. The purpose of this study is verification of the lateral biological dose distribution using modified MKM.

Materials and Methods

The Monte Carlo calculation code of Geant4 simulated a horizontal port at the Heavy Ion Medical Accelerator in Chiba (HIMAC) of National Institute of Radiological Sciences (NIRS) in Japan. Figure 1 shows the schematic view of the beam port. The projectile particle was ¹²C with a kinetic energy of 290 MeV/n, and the 60 mm SOBP was formed by a bar ridge filter made of aluminum. The field size of the broad beam was formed into 10 cmφ using wobbler method and this was controlled to each 10 cm × 10 cm and 5 cm × 5 cm with a multileaf collimator (MLC).

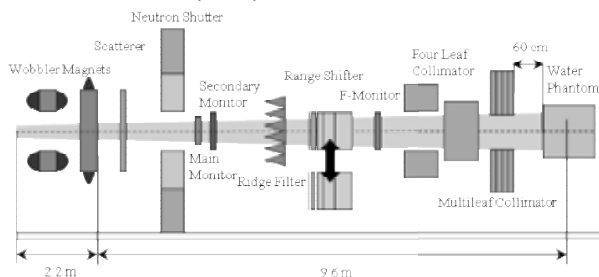


Fig. 1 Schematic view of the horizontal beam port of HIMAC at NIRS for carbon-ion radiotherapy.

The RBE was calculated with the lineal energy spectra measured using tissue equivalent proportional counter (TEPC). The sensitive volume of the commercially available TEPC (LET-1/2, Far West Technology, Goleta CA, USA) was a sphere (diameter: 12.7 mm) filled with a propane-based tissue-equivalent gas (54.6 % C₃H₈, 40.16 % CO₂, and 5.26 % N₂ in mass), which was covered with a spherical wall of A-150 tissue-equivalent plastic (thickness: 1.27 mm). The gas pressure was 4.4 kPa to simulate the energy imparted to a spherical tissue of 1.0 μm diameter. However, the diameter of the TEPC is too large as clinical dosimeter. Therefore, the

size of the small TEPC which was simulated in Geant4 was a half of TEPC (diameter: 6.35 mm) in order to improve position resolution. The tissue-equivalent gas pressure was 8.8 kPa which was double gas pressure of TEPC to simulate a spherical tissue of 1.0 μm. The wall thickness of the small TEPC was 0.914 mm because the effective wall thickness of the small TEPC was equal to that of the TEPC. The lineal energy spectra of the lateral direction for the beam line were simulated at three depths of the proximal (depth = 87 mm), middle (depth = 117 mm), and distal (depth = 143 mm) parts of SOBP, respectively. The lateral RBE₁₀ distributions were calculated with the modified MKM using the simulated spectra. The lateral biological dose distributions were calculated from those lateral RBE distributions and the lateral absorbed dose distributions. The statistical errors of calculations were within 3 %.

Results

Figure 2 shows the comparison of the calculated results with the measurements about the depth absorbed dose distribution and the depth RBE₁₀ distribution where the field size was controlled to 10 cm × 10 cm with MLC.

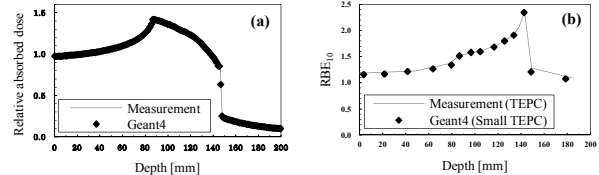


Fig. 2 The depth absorbed dose distribution (a) and the depth RBE₁₀ distribution (b) by measurement and Monte Carlo calculation with Geant4.

Figure 3 shows the comparison of the calculations with the measurements about the lateral absorbed dose distributions. In Figure 2 and 3, those data show the Geant4 calculations were good agreement with the measurements, which indicated that the Geant4 calculations reproduced the experimental conditions.

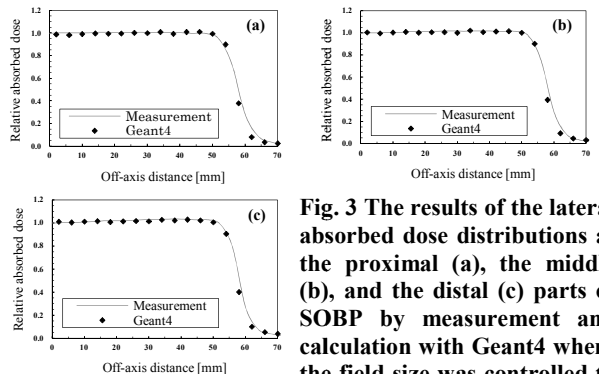


Fig. 3 The results of the lateral absorbed dose distributions at the proximal (a), the middle (b), and the distal (c) parts of SOBP by measurement and calculation with Geant4 where the field size was controlled to 10 cm × 10 cm with MLC.

Figure 4 and 5 show the lateral biological dose distributions and the lateral RBE₁₀ distributions at the proximal, middle, and distal parts of SOBP, where the field size were controlled to 10 cm × 10 cm and 5 cm × 5 cm with MLC respectively.

In Figure 4, the lateral RBE₁₀ distributions were almost constant in the flattened area, and built down in the penumbra region. Also, the flattened area of the lateral RBE₁₀ distribution was decreasing with depth increasing. Therefore, the lateral biological dose distributions were similar to the lateral absorbed dose distributions in the flattened area however the lateral biological dose distributions were smaller than the lateral absorbed dose distributions in the penumbra region.

In Figure 5, the lateral RBE₁₀ distributions where the field size was controlled to 5 cm × 5 cm with MLC were same with the one where the field size was controlled to 10 cm × 10 cm within the error range. The lateral biological dose distributions were also similar to the one where the field size of 10 cm × 10 cm.

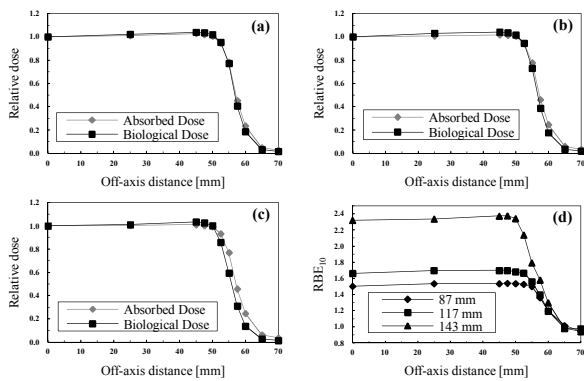


Fig. 4 The results of the lateral absorbed dose and biological dose distributions at the proximal (a), the middle (b), and the distal (c) parts of SOBP and the lateral RBE₁₀ distributions at three depths of SOBP (d) where the field size was controlled to 10 cm × 10 cm with MLC. The vertical axis of absorbed dose and biological dose was normalized with the value at the beam line (Off-Axis Distance = 0 mm).

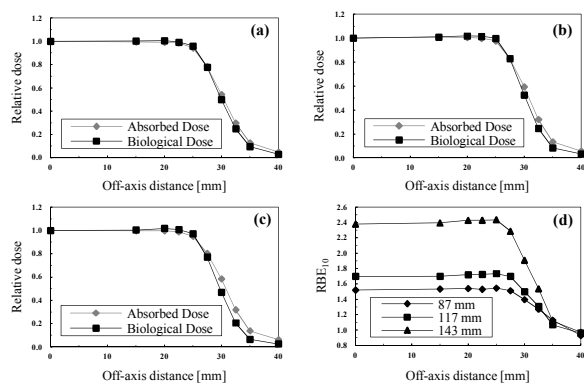


Fig. 5 The results of the lateral absorbed dose and biological dose distributions at the proximal (a), the middle (b), and the distal (c) parts of SOBP and the lateral RBE₁₀ distributions at three depths of SOBP (d) where the field size was controlled to 5 cm × 5 cm with MLC. The vertical axis of absorbed dose and biological dose was normalized with the value at the beam line (Off-Axis Distance = 0 mm).

Discussion

The lateral RBE₁₀ distributions were different for each depth because of the contributions of the energy deposit for the primary particles and the fragment particles. The contributions of the energy deposit for primary particles were investigated considering multiple coulomb scattering. Because the carbon-ions stopped at the proximal part of SOBP penetrate thick part of the bar ridge filter, those particles have large angle scattering at upstream. On the other hand, the carbon-ions stopped at the distal of the SOBP penetrate thin part of the bar ridge filter, those particles rectilinear the irradiation field approximately. Moreover, the fragment particles from the upstream scattering such as hydrogen, helium, lithium, beryllium, and boron, have large angle, in the penumbra region and outside of the irradiation field, the contributions of the energy deposit for those particles were larger than in the irradiation field [3]. That tendency was more notable in the distal part of SOBP. Therefore, the lateral biological dose distributions at the proximal part of SOBP were similar to the lateral absorbed dose distributions. The lateral biological dose distributions at the distal part of SOBP were sharper than the lateral absorbed dose distribution.

The RBE₁₀ at the beam line where the field size was controlled to 5 cm × 5 cm with MLC was larger than the one where the field size was controlled to 10 cm × 10 cm. It was considered that where the field size was large, more fragment particles from off-center region were injected into the beam line. Because they have relatively small lineal energy, the RBE₁₀ decreased. That field size dependencies of radiation quality at the beam line were almost same as the results reported by H. Nose et al. [2]. However, the lateral RBE₁₀ distributions were almost same according to the field size. It was considered that the species of the injected particles had the same ratio of the lateral distributions relatively to the particles injected into the beam line. Moreover, the lateral biological dose distributions were different for each field size. It was considered that the lateral RBE₁₀ distributions were almost same for each field size however the lateral absorbed dose distributions were different.

Conclusions

The lateral biological dose distributions were similar to the lateral absorbed dose distributions in the flattened area. However, in the penumbra region, the lateral biological dose distributions were sharper than the lateral absorbed distributions. Furthermore, that was more notable with depth increasing. Therefore, the field sizes of the biological dose were smaller than the one of the absorbed dose with depth increasing. If the biological effect wasn't taken into account, the lateral dose distributions based on the absorbed dose were overestimated in penumbra region.

References

- [1]Kase Y, Kanai T, Sakama M, Himukai Y, Nose H, Matsufuji N. Microdosimetric Approach to NIRS-defined Biological Dose Measurement for Carbon-ion Treatment Beam. *J. Radiat. Res.* 2011;52:59-68.
- [2]Nose H, Kase Y, Matsufuji N, Kanai T. Field size effect of radiation quality in carbon therapy using passive method. *Med. Phys.* 2009;36 (3):870-875.
- [3]Kusano Y, Kanai T, Kase Y, Matsufuji N, Komori M, Kanematsu N, Ito A, Uchida H. Dose contributions from large-angle scattered particles in therapeutic carbon beams *Med. Phys.* 2007;34 (1): 193-198.

Author address

E-Mail: tamura.mikoto@a.mbox.nagoya-u.ac.jp

THE IMPACT OF SECONDARY PARTICLES ON IN-BEAM PET IMAGING FOR DOSE VERIFICATION IN CARBON ION THERAPY

Su Jung An^{1),2)}, Yong Hyun Chung^{1),2)}

1) Department of Radiological Science, College of Health Science, Yonsei University, Wonju, Republic of Korea
2) Institute of Health Science, Yonsei University, Wonju, Republic of Korea

Introduction

We are developing the C-shaped in-beam PET scanner for dose verification of the carbon therapy. The C-shaped scanner has a ring diameter of 30 cm and an axial field of view of 10 cm for brain imaging. In this design, two detector modules on the incident beam side are removed to avoid blockage of the carbon beam by the detector. During the in-beam PET monitoring of carbon beam delivered by the heavy ion synchrotron, typically, the in-spill data are discarded from the image reconstruction to prevent the degradation of image quality induced by the secondary particles and prompt gamma-rays.

In order to determine the application possibility of the use of data acquired during the beam extraction for PET imaging, we simulated the spatial distributions and yields of the secondary particles and prompt gamma-rays using GATE, and analyzed their influence on the C-shaped PET performances.

Materials and Methods

We simulated carbon beam irradiation on a PMMA (C₅H₈O₂) phantom with 20 cm diameter and 20 cm height using GATE Version 6.1. The carbon beam was delivered horizontally to the phantom, as shown in Fig. 1. 170 AMeV mono-energetic carbon beam was selected and the intensity of the carbon beam was 1×10^8 particles per second (pps).

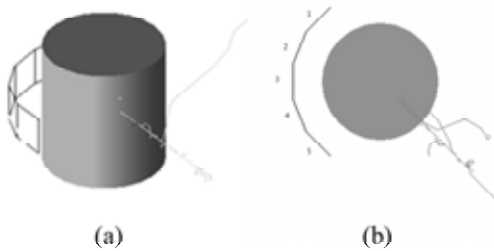


Figure 1. The simulation of carbon beam irradiation

To estimate the spatial emission distributions and yields of the secondary particles and prompt gamma, the five virtual planes which store the phase-space files were positioned at 30.1 cm away from the center of the phantom (Fig. 1). The size of virtual plane is 6×6 cm², and the spacing between planes is 22.5 degree.

To analyze the influence of secondary particles and prompt gamma on PET coincidence image, we obtained the PET images using C-shaped in-beam PET scanner during beam pause and beam extraction, respectively. The simulated C-shaped PET scanner has a ring diameter of 30.2 cm and an axial field of view of 5 cm for brain imaging. To avoid blockage of the carbon beam by the detector modules, the scanner removed two modules on the incident beam side.

The C-shaped scanner consists of 14 detector modules, and each module is composed of an LYSO array of 13×13 elements with a pixel size of $4 \times 4 \times 20$ mm³ and four round PMTs 25.4 mm in diameter. (Fig. 2)

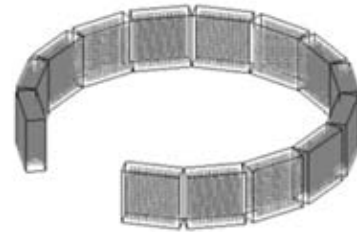


Figure 2. The simulated PET scanner configuration in which the scanner consists of 14 detector modules.

The PET images were obtained based on these assumptions.

- The carbon beam has a tunable time structure given by a repetition of 2 seconds spill length and 3 seconds pause.
- Total therapy time is 2 minutes.
- The PET images are acquired during the total therapy time.

The relative the number of coincidences is calculated.

Results and conclusion

The spatial emission distributions and yields of the secondary particles and prompt gamma were calculated. Fig. 3 shows the simulated flux of secondary particles and prompt gamma for each virtual plane. The major secondary particles produced during carbon beam treatment are neutrons, protons, deuterons and tritons and the dominating contribution to total yield is from neutrons. The secondary particles are mostly emitted toward the direction of the incident carbon beam while the prompt gamma-rays are emitted in all directions with a uniform distribution.

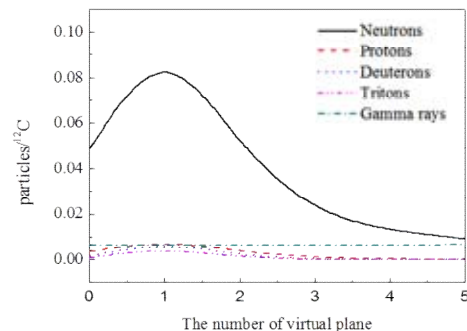


Figure 3. The flux of secondary particles and prompt gamma for each virtual plane.

Table 1. The relative number of coincidences

Effecting radiation	Coincidence
Positron emitter only	100
Positron emitter + neutron	74.51
Positron emitter + deuteron	92.62
Positron emitter + triton	94.42
Positron emitter + gamma	85.53

Table. 1 illustrates the relative number of coincidences showing the influence of the secondary particles and prompt gamma on PET coincidence count during beam extraction. The sensitivity acquired during beam extraction was significantly lower than expected due to random and multiple coincidences by neutrons. To improve image quality by minimizing the effect of neutron, we suggested the use of a partial-ring scanner during beam extraction in which two detector modules on the beam line are inactivated from C-shaped scanner. By using the partial-ring data acquisition during beam extraction, the sensitivity and image quality are significantly improved. This paper provides the basis for a new data acquisition concept to utilize the C-shaped scanner during the beam pause and the partial-ring scanner during the beam extraction for improvement of image quality.

Author address

E-Mail: crystal8374@yonsei.ac.kr

EVALUATION OF RADIATION DOSE TO ORGANS AND TISSUES IN INFANT X-RAY CT

T. Ishii¹⁾, T. Haba¹⁾, S. Kondo¹⁾, D. Hayashi¹⁾, H. Numamoto¹⁾, T. Aoyama¹⁾, S. Koyama¹⁾

1) Department of Radiological Sciences, Nagoya University Graduate School of Medicine, Nagoya, Japan

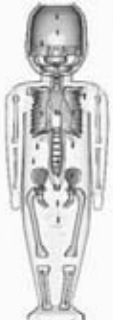
Introduction

X-ray Computed Tomography (CT) examination is a valuable diagnostic technique, and the immediate benefit to the individual patient can be substantial. Evaluations of radiation dose to patients have been absolutely important, because the relatively high radiation doses from x-ray CT compared with other plain radiography have raised health concerns [1]. In particular for infant and children who are more sensitive to radiation than adult, there is the potential increase in future cancer risks from radiation exposure. In this study, the objective was to evaluate absorbed dose for organs of infant undergoing x-ray CT scans by using Monte Carlo simulation. Additionally, organ doses for infant in x-ray CT were measured by in-phantom dosimetry system [2], and compared with the doses calculated by the Monte Carlo simulation.

Materials and Methods

1. Comparison of doses between measurement and simulation

In a whole body X-ray CT scan, organ doses measured in an infant anthropomorphic phantom were compared with organ doses calculated by using Monte Carlo simulation. The Monte Carlo simulation code used for the calculation was Electron Gamma Shower Ver.5 (EGS5). Dose measurements were performed with an in-phantom dosimetry system and non-helical X-ray CT unit TCT-300 (Toshiba Medical Systems, Tochigi, JAPAN). The in-phantom dosimetry system was comprised of an infant anthropomorphic phantom ATOM 703(CIRS, Norfolk, VA) composed of lung, bone, and soft tissue, photodiode sensors, and a data analysis program. Photodiode sensor devices were implanted in the centroid of each organs and tissues. Organ and tissue doses were obtained from calculations by the analysis program based on output voltage resulting from the photodiode sensors. The number of the photodiode sensor device is 24, and Fig.1 shows correspondence relation between the devices and the organs and tissues.



Number of sensors and organs			
ch1	Brain 1	ch13	Stomach
ch2	Brain 2	ch14	Colon
ch3	Lens	ch15	Lumbus
ch4	Salivary gland	ch16	Coxae 1
ch5	cervical spine	ch17	Colon sigmoideum
ch6	Thyroid gland	ch18	Bladder
ch7	humerus	ch19	Ovary
ch8	Heart	ch20	Femur
ch9	Lung	ch21	Rctcolon
ch10	Breast	ch22	Testis
ch11	Esophagus	ch23	Skin 1
ch12	Liver	ch24	Skin 2

Fig.1 Anthropomorphic phantom of infant. The number of photodiode x-ray sensors implanted in phantom and each position of tissues and organs.

In the simulation, X-ray CT scanning geometry was same as the measurements. A voxelized mathematical phantom (voxel phantom) was developed based on the X-ray CT images of the infant anthropomorphic phantom. The voxel phantom containing photodiode sensor regions was incorporated into the simulation. The sensor regional doses were calculated as each corresponding organ. These calculated organ doses were compared with measurements, and the Monte Carlo simulation was verified.

2. Calculation of average dose in the organs installed in the anthropomorphic phantom

The organ doses in the voxel phantom were obtained by the above simulation method, however, these doses were evaluated in each small region in the centroid of the organs. Each organ has some volume, and the organs which have the volume based on a Japanese standard were incorporated in the voxel phantom. Fig.2 shows an image of the voxel phantom. The organs and tissues labels were assigned correctly to the value of each voxel in reference to the weights of the organs in normal Japanese [3]. The absorbed energy doses for entire target organs were evaluated. The calculations and measurements were carried out for head CT and thoracoabdominal CT.

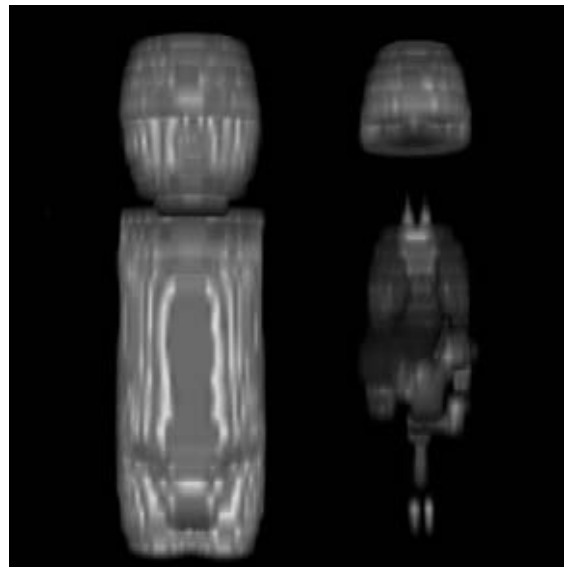


Fig.2 The infant voxelized mathematical phantom. Image of the form (left) and incorporated organs and tissues (right).

Results and discussion

Fig.3 shows comparison of the absorbed doses in each photodiode sensors positions between the measurement and the simulation undergoing X-ray CT examination. The measured dose and the calculated dose in each position in the phantom were agreed within average error $\pm 8.0\%$. The maximum difference channel was at the ch 20, and the difference was about 14%. The error of dose estimation depends on the dosimetry system in the measurement and statistical error associated with calculated photon number in the simulation. In the dosimetry system, a measure cause of the error was attributed to conversion from detector output to absorbed dose. This error was estimated within about $\pm 6.0\%$ by prior experimental research. In the calculation, statistical error was within $\pm 7.0\%$. In the incorporation of the organs and tissues in the voxel phantom, size and location were important factors.

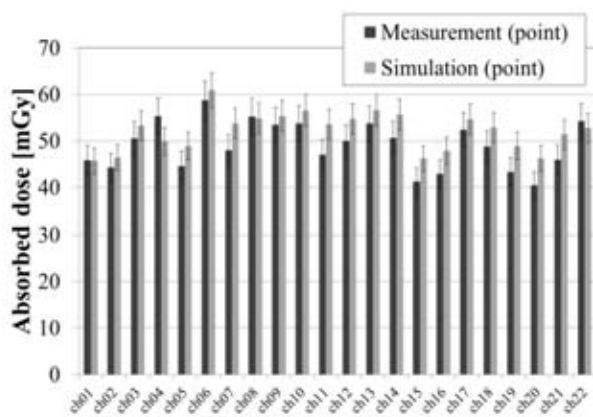


Fig.3 Comparison of the absorbed energy doses between measurement and simulation in points.

Fig.4(a) shows comparison of the absorbed doses in organs and tissue between measurement and simulation undergoing a head CT scan. The calculated organ doses based on the average doses for entire target organs and the measured organ doses based on the absorbed doses in each centroid points of organs and tissues were agreed within average difference of $\pm 16\%$. The maximum difference organs was bone marrow. This error was due to a difference in location of the evaluation point. In the simulation, bone marrow was distributed over the whole inside of the bones of 1mm the voxel phantom. In the measurement, the dose for bone marrow was evaluated by three photodiode sensor devices implanted in the brain and the salivary gland.

Fig.4(b) shows comparison of the absorbed doses in organs and tissues between measurement and simulation undergoing a thoracoabdominal CT scans. Within the scan range, the calculated average doses in the whole organs and the measured point dose were agreed within average difference of $\pm 15.0\%$. In the organs such as thyroid and testis located near the both ends of scan range, the calculated doses were higher than measured doses. In the calculation, the organ was partially irradiated in the end of the scan area. In the measurement, however, the photodiode sensors for these organs were located out of scan range, the absorbed doses for these organs.

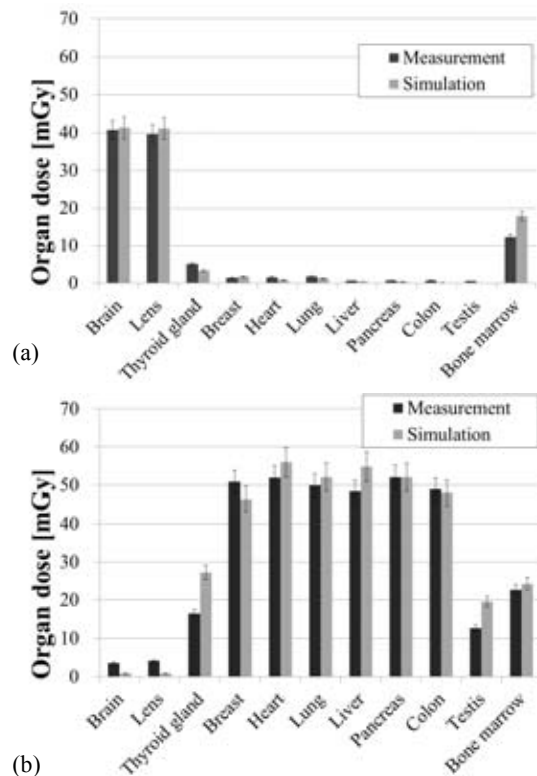


Fig.4 Comparison of the organ doses between measurement and simulation in (a) head (b) thoracoabdominal CT scans.

Conclusions

For measurements, some organ doses are evaluated by the absorbed energy in each center points of tissues and organs which is small points. Using Monte Carlo simulation, organ doses for infant were calculated and evaluated based on absorbed energy doses for entire target organs. In this study, we reaffirmed utility of the dosimetry systems and computer simulation in evaluation for radiation doses.

References

- [1] International Commission on Radiological Protection, "The 2007 Recommendations of the International Commission on Radiological Protection," ICRP publication 103, Annals of the ICRP 37 (2007).
- [2] T. Aoyama, S. Koyama, C. Kawaura, "An in-phantom dosimetry system using pin silicon photodiode radiation sensors for measuring organ doses in x-ray CT and other diagnostic radiology," *Med. Phys.* **29**, 1504-1510, (2009).
- [3] G. Tanaka, Y. Nakahara, Y. Nakazima, "Japanese Reference Man 1988-IV -Studies on the Weight and Size of Internal Organs of Normal Japanese-," *JRS.* **49**(3), 344-364, (1989)

Author address

E-Mail: ishii.takanori@a.mbox.nagoya-u.ac.jp

DIGITAL BREAST TOMOSYNTHESIS AND DIGITAL MAMMOGRAPHY – A COMPARISON OF FIGURES OF MERIT FOR VARIOUS AVERAGE GLANDULAR DOSES

Y.S.Kim¹⁾, H.S.Park¹⁾, S.J.Park¹⁾, J.G.Choi²⁾, Y.W.Choi²⁾ and H.J.Kim*¹⁾

1) Department of Radiological Science and Research Institute of Health Science, Yonsei University, Wonju, Korea
2) Pioneering Medical-Physics Research Center, Kora Electrotechnology Research Institute (KERI), Ansan, Korea

Introduction

Breast cancer is a disease in which malignant cancer in the tissues of the breast. One in eight women get breast cancer in their lives and breast cancer is the second leading cause of women cancer death [1]. Digital mammography (DM) has been credited as one of the major reasons for the early detection to decrease in breast cancer mortality in the last 20 years. However, DM is still far from perfect for several limitations [2]. Most patients can be uncomfortable and occasionally painful due to the breast compression during the screening mammography and the two dimensional projection can degrade the lesion conspicuity due to the overlapping suspicious lesion and fibroglandular tissue. The digital breast tomosynthesis (DBT) system can provide 3D information with a limited number of cone-beam projections and therefore reduce the obscuring effect of breast tissue overlap in screening mammography for the improved margin visibility and early detection of breast cancer [3]. In addition to the reduction of structure noise contribution, DBT system makes depth localization possible and requires the smaller dynamic range for each reconstructed slice .

The aim of the study is to compare the performance of DBT with DM system. We acquired a CC view from DM system and reconstructed images from DBT system with breast tissue equivalent phantom designed for three dimensional breast imaging. The average glandular dose used for image acquisition was from 1 mGy to 4 mGy. The figure of merit (FOM) and measurement accuracy of lesion size were evaluated and discussed in this study.

Materials and Methods

1. Image acquisition system

The mammography system used in this study was described in figure 1 (a) (Brestige, MEDI-FUTURE, Korea). The detector type is TFT-based direct conversion full-field flat-panel digital detector and the x-ray absorption material is amorphous selenium (a-Se). The DBT was performed on a prototype unit (KERI DBT system, KERI, Korea) shown in figure 1 (b). The system developed by KERI (Korea electrotechnology research institute) has not been yet commercially available in Korea and its clinical application is under preparation. The DBT prototype is equipped with an CsI phosphor/CMOS flat panel detector (2923MAM, Dexela Ltd., UK) optimized for very low exposures with rapid readout. Images were acquired from 15 different angular position using a prototype DBT system and one projection from 0° with a DM system. The reconstructed algorithm used is based on separable paraboloidal surrogates and is related to the maximum-likelihood expectation-maximization (ML-EM) algorithm. The reconstructed slice thickness is 1 mm and the reconstructed image matrix is 4025 ×2006. Five iterations were used for all reconstruction.

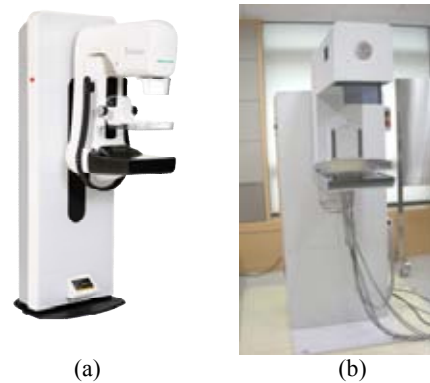


Figure 1. Digital mammography system (a) and prototype digital breast tomosynthesis system(b) description

2. Average glandular dose (AGD)

For conventional DM, the average glandular dose (AGD) is estimated using

$$D=K \cdot g \cdot c \cdot s \quad (1)$$

where K is the incident air kerma at the surface of breast phantom and factor g, c and s are conversion factors tabulated by Dance et al[4].

Average glandular dose proposed for DBT was calculated using a formalism, which is a simple extension of the UK, European and IAEA protocols for dosimetry in conventional DM introduced by D. Dance et al (2011) [5]. The formalism

$$D_T=K_T \cdot g \cdot c \cdot s \cdot T \quad (2)$$

is proposed. For a 3D breast dose, D_T gives the average glandular dose for total projections acquired at total angular span. The incident air kerma K_T is measured with the sum of mAs for the examination in the straight through position which projection angle is 0°. The factor T gives ‘tomo’ factor for different scan ranges against breast thickness [5].

3. Image analysis

The traditional Figure of Merit (FOM) used in diagnostic radiology to optimize the signal detectability used previously by other authors is given by

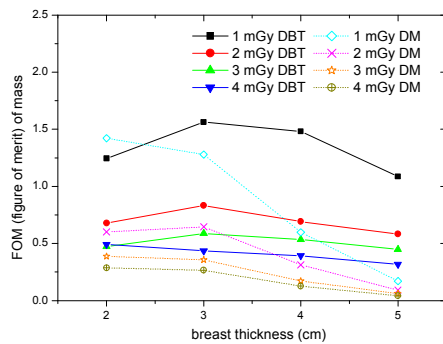
$$FOM=CNR^2/AGD \quad (3)$$

In above equation, the denominator is the average glandular dose, which is directly proportional to the patient stochastic radiation risk. The value of FOM is independent of the number of photons, and relates solely to differences in the radiation quality. Therefore, the optimum imaging condition is found at exposure conditions where FOM is at its maximum.

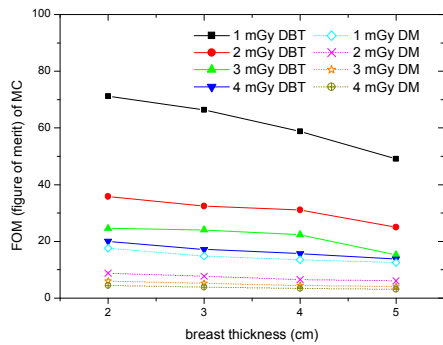
Results

To compare the results quantitatively, the contrast and CNR were calculated with the in-focus plane from DBT reconstruction image and CC images from DM system.

Seen in figure 2 are plots of FOM as a function of breast thickness (cm) for DBT and DM. The results of mass as shown in figure 2 (a) exhibit the highest FOM acquired with 1 mGy of AGD by DM system and the DBT system provides second highest FOM with 1 mGy of AGD. However, as increasing the breast thickness, the results of DM system decrease sharply. In result of 5 cm of breast phantom, overall FOM of DBT system is superior to that of DM system. Figure 2 (b) shows the FOM of micro-calcification acquired with each volume of breast. As noticeably high CNR of DBT influences on the results of FOM, the FOM of micro-calcification acquired with DBT system is superior to that acquired with DM system and the highest FOM is exhibited with DBT system with 1 mGy of AGD.



(a)



(b)

Figure 2. The traditional FOM measured for different thickness of breast: (a) mass and (b) micro-calcification

Figure 3 shows the magnification for the micro-calcification details acquired with DM (a) and DBT system (b). The number of micro-calcification observed is same with both systems and evident superiority in visibility of calcification is not demonstrated.

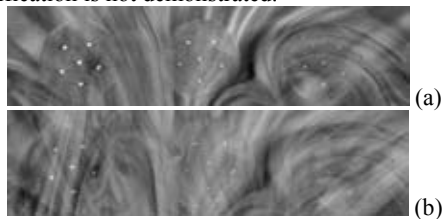


Figure 3. MC details acquired with DM(a) and DBT (b)

On the other hand, better conspicuity of mass is clear observed in the image acquired with DBT system as shown in figure 4. Figure 4 (a) shows the magnification for the mass

details with DBT system and figure 4 (b) shows mass details acquired with DM system.

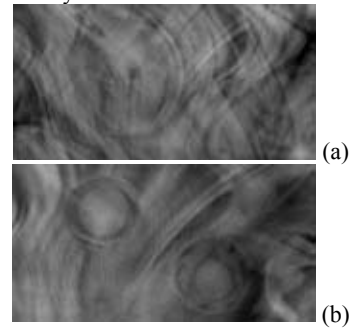


Figure 4. Mass details acquired with DM(a) and DBT (b)

Discussion

FOM provides the optimal exposure condition and imaging system as a function of breast thickness, that is to say, high quality image in low glandular dose derives high FOM result. As shown in figure 5, for thin breast (e.g. 2 cm of breast phantom), DM system with 1 mGy of AGD provides the highest FOM of mass result due to the reduction of overlapping normal breast tissue and lesion. The FOM of mass with DM system decreases sharply as increasing breast thickness due to the increase in the effects of anatomical noise as shown in CNR result. As compared with DM, DBT system acquires slices at each depth and this reduces the influence of anatomical noise.

This study, with further studies and limitations, demonstrates the potential of DBT system for early detection of breast cancer and contributes to the development of DBT system and clinical application.

Conclusions

In this study we compared the performance of DM and DBT system with different AGD and breast thickness. Although the DM showed higher FOM of mass with thin breast due to the reduced anatomical noise, increasing breast thickness causes the superiority of FOM with DBT system over DM system. For the micro-calcification detection, the DBT system showed significantly higher FOM and led more accurate measurement of the micro-calcification size than DM system. Moreover, the visibility of lesions, especially for low contrast of mass, in thick breast was better with DBT system. In conclusions, these results indicated that DBT system plays an important role in early detection of breast cancer especially for dense breast.

References

- [1]Christina MS, Ehsan S, Robert SS, Moustafa Z, Joseph YL. Toward Quantification of Breast Tomosynthesis Imaging. Proc. of SPIE. 2008; 6913: 69134N.
- [2]J Zhou, B Zhao, W Zhao. A computer simulation platform for the optimization of a breast tomosynthesis system. Med. Phys. 2007;34(3):1098-1109.
- [3]JM Park, EA Franken, M Garg, LL Fajardo, LT Niklason. Breast Tomosynthesis:Present Considerations and Future Applications. RadioGraphics. 2007;27:S231-S240.
- [4]DR Dance, CL Skinner, KC Young, JR Beckett, CJ Kotre. Additional factors for the estimation of mean glandular breast dose using the UK mammography dosimetry protocol. Phy. Med. Biol. 2000;45:3225-3240
- [5]DR Dance, KC Young, RE van Engen. Estimation of mean glandular dose for breast tomosynthesis: factors for use with UK, European and IAEA breast dosimetry protocols. Phys. Med. Biol. 2011;56:453-471

Author address

E-Mail: yeskim@yonsei.ac.kr

REDUCTION OF PATIENT DOSE IN DIGITAL MAMMOGRAPHY :SIMULATION OF LOW-DOSE IMAGE FROM ROUTINE-DOSE

Yuki Saito¹⁾, Maki Sakai²⁾, Naotoshi Fujita³⁾, Yoshie Kodera¹⁾

1) Department of Radiological Sciences, Nagoya University Graduate School of Medicine, Nagoya, Japan

2) Department of Radiological Technology, Nagoya Daini Red Cross Hospital, Nagoya, Japan

3) Department of Radiological Technology, Nagoya University Hospital, Nagoya, Japan

Introduction

To reduce patients' exposure to radiation during digital mammography, it is preferable to acquire images using a minimum dose. Recently, owing to the developments of X-ray detectors, the exposure dose required for acquiring a digital image has been re-examined. It is necessary to assess several low-dose images in order to establish a diagnosis. However, it is clinically undesirable to expose a patient to several exposure conditions for determining an optimal image. Therefore, it is necessary to generate a low-dose image through simulation.

The purpose of this study is to simulate a low-dose image from the image generated using a routine-dose. The noise in an image varies because the detected photons pass through materials consisting of different substances and having varying thicknesses. Hence, it is necessary to add a different noise to each pixel value in the image. The aim of this study is the addition of a different noise for each pixel by considering the resolution of the X-ray detector.

Materials and Methods

1. Materials

This study used the digital mammography system with different detectors. It is computed radiography (CR) system and flat panel detector (FPD) system. The CR reader used was a REGIUS V stage, Model 190. The CR plate used was CP1M200 with columnar crystal photostimulable phosphor. Pixel pitch of CR reader is 43.75 μm . These were manufactured by Konica Minolta MG. And, FPD system is Hologic Selenia with an amorphous selenium detector with pixel pitch of 70 μm .

2. Simulation process

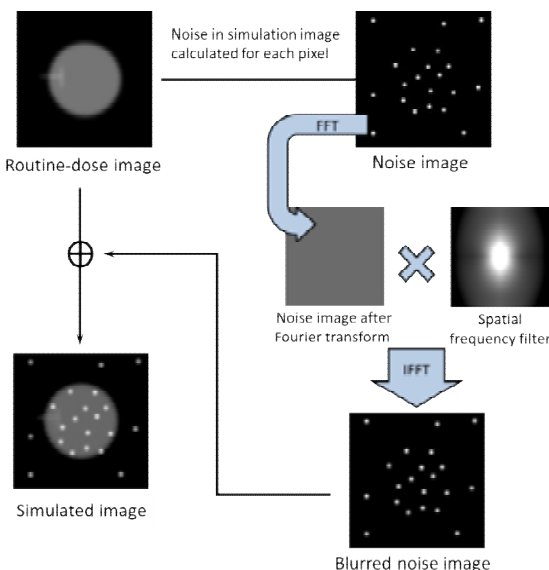


Fig.1 Flow-chart of the simulation process

Figure 1 shows a flow-chart of the simulation process. The noise image that accounts for the pixel value of the low-dose image is generated from the relationship between the pixel value and the standard deviation (SD), which serves as the noise index. The noise is calculated for each pixel value, based on the variation in detected photons of a routine-dose image. The noise is blurred by the resolution of the X-ray detector in a spatial frequency domain. The blurred noise image is added to the routine-dose image to generate the simulation image.

3. Generation of additional noise

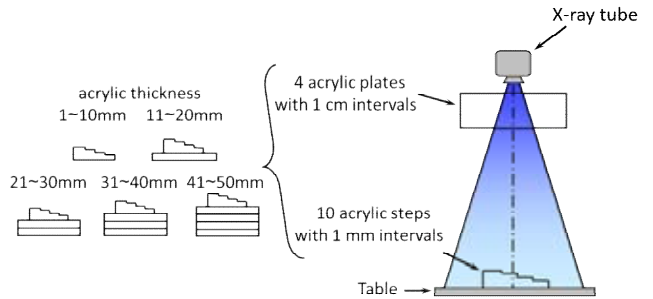


Fig.2 Experimental setup

Images of the acrylic steps were obtained to examine the relationship between the pixel value and the noise. The experimental setup is shown in Fig. 2. It included 10 acrylic steps spaced at 1 mm intervals and four acrylic plates spaced at 1 cm intervals. By employing both acrylic steps and acrylic plates, images with up to 50 acrylic steps placed at 1mm intervals were obtained. Ten different exposure doses were established through digital mammography. Next, the images were generated under 500 different exposure conditions. We measured the pixel value under each exposure condition and calculated the SD as the noise index. Under all exposure conditions, the tube voltage was 28 kV and the target/filter was Mo/Mo.

4. Take into account detector resolution

The noise made was approximated to the Gaussian noise, and variations in dosage resulted in changes in SD. The simulation noise became identical to the value of the Wiener spectrum (WS) ranging from a low frequency to a high frequency. However, the actual shape of the WS changed on the basis of the modulation transfer function (MTF) of the imaging system in equation (1).

$$WS(u) \propto \frac{\gamma^2 |MTF^2(u)|}{|n|} \quad (1)$$

Thus, a spatial frequency filter was designed using the MTF. The shape of the WS was corrected using the following filters. The first filter was designed based on the presampled MTF, the second was designed based on the digital MTF containing aliasing, and the third was designed based on the measured value of the WS.

Results

1. Relationship between the pixel value and the noise

We determined relationship between the pixel value and the SD of the acrylic steps. It can be seen relationship of the CR system of that the SD decreases as the pixel value increases. On the other hand, it can be seen from relationship of the FPD system that the SD increases as the pixel value increases. But relationship of the CR system is non-linear imaging system, and has a logarithmic amplifier. Then, relationship of FPD system transformed to the non-linear date when the SD decreases as the pixel value increases. The difference between the pixel values of the routine-dose and low-dose images freely fluctuates with the mAs value of the low-dose image to be simulated. And SD was calculated for each pixel.

2. Comparison of phantom images

The 50 mAs image was used as the routine-dose image, and the low-dose image of 10 mAs by both systems was obtained through simulation. We simulated the images using a tissue-equivalent mammography phantom of CIRS Model 012A. Figure 3 shows the actual low-dose image of 10 mAs by CR system, Fig. 4 shows the image simulated using the filter based on the WS of CR system, Fig. 5 shows the images actual low-dose image of 10 mAs by FPD system, and Fig. 6 shows the image simulated using the filter based on the digital MTF of FPD system. The image simulated using the filter based on the WS is similar to the actual low-dose image by both systems. The noise suitable for the generation of the low-dose image could be easily transferred to the routine-dose image. The image simulated using the presampled MTF filter is very different from the actual low-dose image by CR systems. And, we consider the image simulated using the digital MTF filter was closer to an actual low-dose image compared to the image simulated using the presampled MTF filter of CR systems. But the image simulated using the digital MTF filter of FPD system was similar to an actual low-dose image.

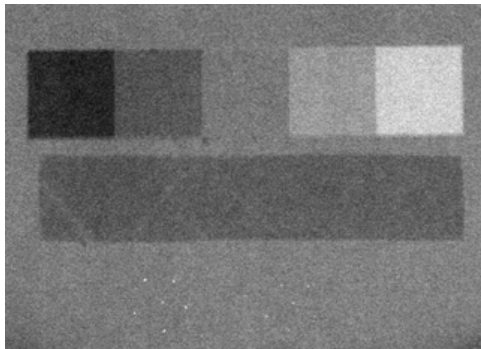


Fig.3 The images actual low-dose image of 10 mAs by CR system

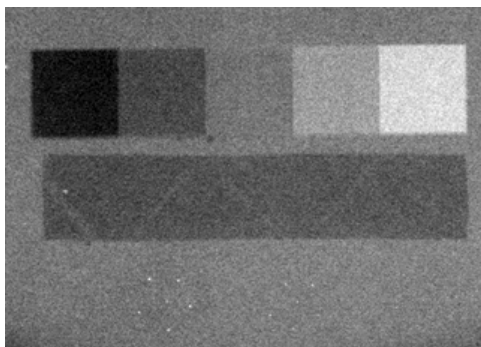


Fig.4 The image simulated using the filter based on the WS of CR system

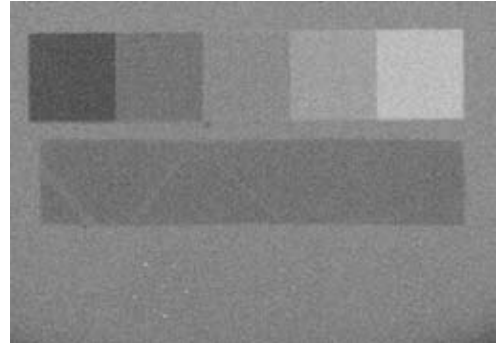


Fig.5 The images actual low-dose image of 10 mAs by FPD system

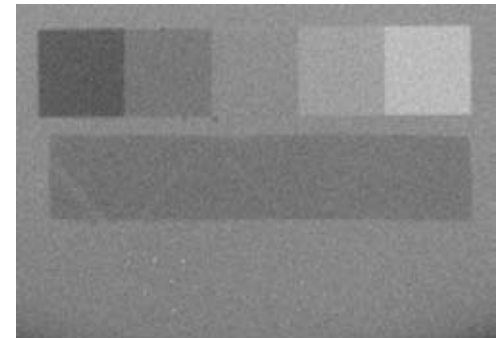


Fig.6 The image simulated using the filter based on the digital MTF of FPD system

Discussion

The image simulated using the presampled MTF filter is less similar to the actual low-dose image by CR system. Since the MTF value is high, the CR plate used in this case was developed for mammography and influences the aliasing in the image. Therefore, the image simulated using the digital MTF filter is close to an actual low-dose image. In addition, when using the digital MTF filter, it is better to divide noise sources. This is because certain noise is influenced by the resolution of the X-ray detector (e.g., quantum noise) while certain other noise is not (e.g., structure noise). In addition, the dominant noise component depends on the amount of photons absorbed by the X-ray detector. We believe that the simulation becomes even more precise when the additional noise is also divided into noise sources.

Conclusions

By using the proposed method, we were able to obtain a simulated low-dose image from an image generated by a routine-dose. This method is expected to facilitate a low-exposure condition for generating an image of sufficient quality and lead to reduced dose exposure to patients.

References

- [1] M. B ath, M. H akansson, A. Tingberg, L. G. M ansson, Method of simulating dose reduction for digital radiographic systems, *Radiation Protection Dosimetry*, 2005;114: 253-259.
- [2] W. J. H. Veldkamp, L. J. M. Kroft, J. Pieter A. V. Delft, J. Geleijns, A Technique for Simulating the Effect of Dose Reduction on Image Quality in Digital Chest Radiography, *Journal of Digital Imaging*, 2009;22-2; 114-125.

Author address

E-Mail: saitoh.yuuki@e.mbox.nagoya-u.ac.jp

Optimization of the angle between detector modules in a dual-head cardiac SPECT

Woo Jin Jo^{1,2)}, Yong Hyun Chung^{1,2)}

1) Department of Radiological Science, College of Health Science, Yonsei University, Wonju, Korea
2) Institute of Health Science, Yonsei University, Wonju, Republic of Korea

Introduction

In the early days of SPECT imaging, it was performed by rotating a single-head Anger camera to obtain projection data from multiple angles. With advances in instrumentation and software, alternative designs have been developed and commercialized such as the use of multi-head systems that allow simultaneous acquisition of multiple-projection views [1-2]. Multi-head cameras can be constructed using a variety of configurations, with 2 or 3 heads angled at 90°, 120°, or 180°. This set-up allows for improved image quality by reducing the image acquisition time or increasing the total counts compared with a single-head camera [3]. Since the heart is located in the left side of the thorax, gamma rays are highly attenuated in the posterior projections from left posterior oblique (LPO) to right anterior oblique (RAO) angles [4]. To minimize tissue attenuation, projections are usually obtained using 180° acquisition that extends from the LPO to the RAO view. Therefore, current standard protocol for myocardial perfusion SPECT is 180° acquisition with a 90° dual-head system [5]. The optimal angular displacement between detector heads in dual-head SPECT remains controversial, however, because it depends on both the size of the patient and the detector. It is necessary to explore the relationship between image quality and the angle between detector heads to minimize the distance between the heart and the detector head.

In this study, the effect of the angle between detector heads in small-animal dual-head SPECT on cardiac image quality was investigated through Monte Carlo simulations. Prior to these simulations, we validated the GATE simulator experimentally.

Materials and Methods

Small animal SPECT system for simulator validation study: The detector used in the simulator validation was composed of a 50 x 50 x 6 mm³ monolithic NaI(Tl) crystal coupled to a position-sensitive photomultiplier tube (Hamamatsu, H8500), a parallel-hole collimator, the frontend electronics, a data acquisition system, and a motorized rotating stage as shown in Figure 1(a). The crystal and PSPMT were mounted in the metal housing with lead shielding against background radiation. The lead parallel-hole collimator was 35 mm thick and consisted of a 1.5 mm diameter hexagonal hole with 0.2 mm septa. The 64-channel anode signals of PSPMT were routed to the resistive anger logic circuit (Vertilon, SIB064-1018) to generate four positioning outputs. These outputs connected to a Vertilon PhotoniQ IQSP418 multichannel data acquisition system via four coaxial cables.

Experimental measurements were carried out using a 28 μCi ⁵⁷Co point source on the rotation stage. The distance between the center of rotation and the collimator surface was 20 mm as shown in Figure 1(b). SPECT data acquisition time was 8 minutes per projection, and the data were collected at 2° increments over 180° in step-and-shoot mode. Imaging was performed using a 20% energy window centered on the 122 keV photopeak of ⁵⁷Co. The filtered back projection with a Hanning filter was used to reconstruct tomographic image.

System sensitivity was measured and reconstructed spatial resolution was calculated using Gaussian fit on the count profile from the point source.

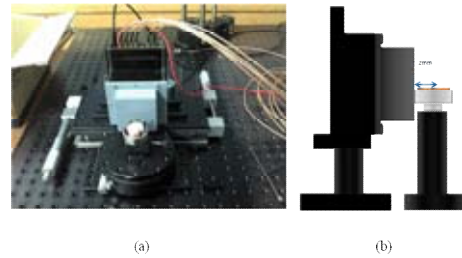


Figure 1. SPECT system developed for simulator verification. This module was composed of H8500 PSPMT, NaI(Tl) scintillation crystal, a parallel hole collimator, and an object rotating stage (a). The distance between the center of rotation and the collimator was 20 mm (b).

The simulation was performed using GATE version 3.1.2 based on the GEANT4 toolkit. The detector was modeled according to geometrical characteristics as described above. In order to reduce the computation time, two detector heads were simulated and the activity of the source was set to 5 mCi. Projection data for 90 views was acquired over a 180° step-and-shoot acquisition, with a 1 sec acquisition per projection.

Effect of the angle between scanner heads on cardiac image quality: To characterize the relationship between image quality and the angle between scanner heads, dual head SPECT was simulated by varying the angle between heads as 70°, 80°, 90°, 100°, and 110°. Each detector head consists of a 50 x 50 x 6 mm³ NaI(Tl) optically coupled to a Hamamatsu H8500 PSPMT and a parallel-hole collimator as described previously. The distance between the collimator surface and the center of rotation were set to 20, 20, 20, 25, and 31.5 mm for 70°, 80°, 90°, 100°, and 110°, respectively, using a 40 mm field of view (FOV) as shown in Figure 2.

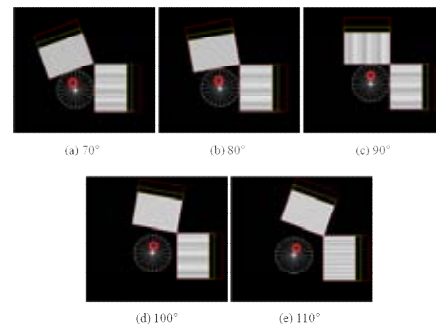


Figure 2. Simulation geometry of the dual-head SPECT systems with an angle between the detector heads of 70° (a), 80° (b), 90° (c), 100° (d), and 110° (e).

The mouse myocardium phantom was modeled as a cylinder with an outer diameter of 10 mm, wall thickness of 2.7 mm, and height of 5 mm in a water-filled cylindrical phantom 4 cm in diameter and 3 cm in height. The myocardium phantom was filled with water and 1.5 mCi ^{99m}Tc-99, and the projections were obtained using 180° acquisition that extended from the LPO to the RAO view. Projection data from 110, 100, 90, 100 and 110 views were acquired in 2° increments over 180° for the angles of 70°, 80°, 90°, 100°, and 110°, respectively, between

heads. The tomographic image was reconstructed using a filtered back projection algorithm, and its quality was evaluated by measuring the myocardial wall to cavity ratio.

Results

Simulator validation study: Figure 3 shows the simulated and measured SPECT images obtained using a point source at the center of rotation. Spatial resolution defined as a full width at half maximum (FWHM) of the point source profile, and sensitivity defined as the ratio between source activity and the total number of events were calculated as shown in Table 1. There were no significant differences between simulated and measured results. The relative error of the spatial resolution and sensitivity were 5.7% and 8.4%, respectively.

	Measurement	Simulation	Relative error
FWHM (mm)	3.7	3.5	5.7%
Sensitivity(cps/MBq)	167	181	8.4%

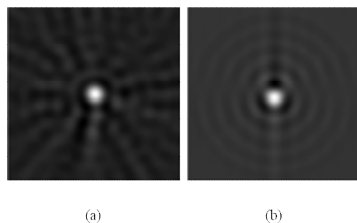


Figure 3. Simulated and measured point source image. Computer simulated (a) and experimental results (b).

Effecto of the angle between heads on cardiac image quality: Figure 4 shows the SPECT images of the mouse myocardium phantom obtained by varying the angle between heads and their horizontal profiles. The x-axis represents the pixel size (0.25 mm per pixel) and the y-values were normalized to the maximum pixel value. When the angle between heads exceeded 90°, images of the myocardium were blurred by the increased distance between the phantom and the detector head. The myocardial wall and cavity were most clearly distinguished at an angle between heads of 80°.

In order to find the best angle between heads, the angular displacement was subdivided and additional simulations were performed at 76° and 84°. The peak to valley ratio representing the wall to cavity ratio was measured for 18 angular directions with 10° intervals, and the mean and standard deviation were calculated.

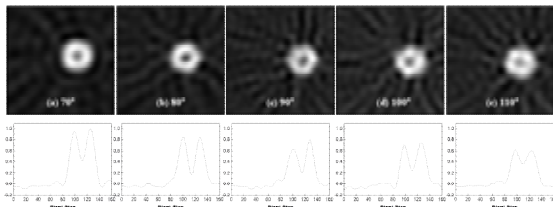


Figure 4. Myocardium phantom images and their profiles acquired by varying the angle between detector heads.

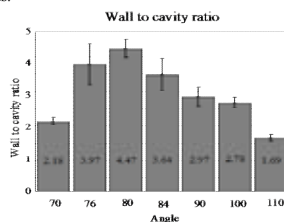


Figure 5. The mean and standard deviation of myocardial wall and cavity ratio for the angle between heads of 70°, 76°, 80°, 84°, 90°, 100° and 110°.

As shown in figure 5, the myocardial wall to cavity ratio was measured as 2.18, 3.97, 4.47, 3.64, 2.97, 2.78 and 1.69 for angles between heads of 70°, 76°, 80°, 84°, 90°, 100° and 110°, respectively. An 80° arrangement of the detector heads in this system generated the best wall to cavity ratio.

Discussion

In this paper, we presented validation results for use of the GATE simulator based comparisons of simulated versus experimental measurements acquired using a small-animal SPECT system. Spatial resolution and sensitivity were evaluated using a ⁵⁷Co source, and overall results were within 10% accuracy between the simulated and acquired SPECT images.

Dual-head cardiac SPECT for small animal imaging was simulated using a validated GATE model to characterize the imaging performance as a function of the angle between the two detector heads. Consequently, an angular displacement of 80° provided the highest quality myocardial image in the simulation. This is the result of the cardiac geometry shifting to one side. This leads to a change in source-to-detector distance, which affects scatter and attenuation. As a result, image quality characteristics were varied depending on the angle between heads.

In this study, the surfaces of both heads were close enough to each other to only consider the effects of the angle between heads. In the actual dual head SPECT system, however, if both camera heads are at an angle of exactly 90° to each other, part of the patient lies outside of the field of view. For this reason, one manufacturer provides SPECT acquisitions with heads at a 76° angle to each other. [6]

In order to obtain meaningful 180° information using the dual head SPECT system, the number of projections was varied according to detector angle. For example, in 70° and 110° angle geometry, 110 projections were acquired, in 80° and 100° angle geometry, 100 projections were acquired, and in 90° angle geometry, 90 projections were acquired. As a result, data acquisition time was increased in 70°, 80°, 100° and 110° angle geometry compared with 90° angle geometry. This increase in acquisition time was not significant (approximately 10% of the total acquisition time).

Conclusions

The dual heads at an 80° geometric angle produce the highest quality myocardial images in our small animal SPECT system. This is the optimal angle between detector heads that maximizes image quality in cardiac SPECT. Since the optimum angle geometry also depends on patient body type, preparing a protocol for patients with a particular body habitus will be helpful in acquiring optimum myocardial SPECT images without additional hardware.

References

- [1]Jonathan M. Links, Eur J Nucl Med. 20, 440 (1993)
- [2]Links JM, Frank TL, Engdahl JC et al, Eur J Nucl Med. 6, 548 (1995)
- [3]Travin MI, Semin Nucl Med. 3, 182 (2011)
- [4]Einsner RL, Nowak DJ, Pettigrew R et al, J Nucl Med. 11, 1717 (1986)
- [5]Tracy L. Faber, J nucl Cardiol. 3, 292 (1994)
- [6]Jerrold T, Bush berg, "The Essential Physics of medical imaging", p712

Author address

E-Mail: wincom@yonsei.ac.kr

ACCURACY OF 3D CINE PHASE CONTRAST MR FLOW MEASUREMENT FOR COMMON CAROTID ARTERIES

Ikki Tozawa¹, Haruo Isoda¹, Atsushi Fukuyama¹, Kento Morita², Katsuya Maruyama³, Yoshiaki Komori³, Toshiyasu Shimizu⁴, Takashi Kosugi⁴, Yasuo Takehara⁵, Shinji Naganawa⁶

¹ Department of Radiological Sciences, Nagoya University Graduate School of Medicine

² Department of Radiological Technology, Nagoya University School of Health Sciences

³Siemens Japan K.K.

⁴Renaissance of Technology Corporation

⁵Department of Radiology, Hamamatsu University School of Medicine

⁶ Department of Radiology, Nagoya University Graduate School of Medicine

Introduction

Hemodynamics plays a very important role in the initiation and progression of vascular diseases [1]. Therefore, it is important to evaluate the blood flow in the vessel accurately. Doppler ultrasound is a common method for the evaluation of carotid arterial hemodynamics, however it has low operator reproducibility and its coverage of the sample volume within the vessel is limited. Hemodynamic analysis by two-dimensional phase contrast MR imaging (2D cine PC MRI) has also been used. Recently, 3D cine PC MRI [2], which provides us with temporal three directional and three dimensional flow information, has been used for evaluation of hemodynamics of the carotid artery. This promising imaging technique has not been fully utilized in clinical practice as its accuracy has not been adequately verified.

The purpose of this study was to investigate the effects of spatial resolution on the accuracy of 2D and 3D cine PC MR flow measurement with the aid of a carotid arterial phantom, and to evaluate of the accuracy of 3D cine PC MRI of the common carotid artery (CCA) of healthy volunteers using the results of existing 2D cine PC MRI as a gold standard.

Materials and Methods

Our flow phantom was an acrylic tube with a 6 mm inner diameter mimicking a CCA. We ran a 40 % glycerin solution with a steady flow (30 cm/s) using a pump (Nemo pump NHL29PUA; Heishin Ltd., Kobe, Japan). The flow rate was measured with a digital Coriolis flowmeter (FD-SF1; Keyence Corporation, Osaka, Japan; 2% error in the range of 200ml/min to 500ml/min). We performed 2D and 3D cine PC MRI with prospective pseudo ECG gating using 3T MR system (MAGNETOM Verio 3T; SIEMENS, Erlangen, Germany) with neck matrix coil. We set the spatial resolutions at 0.63 to 2.5 mm for 2D cine PC MRI and 0.67 to 2.0 mm for 3D cine PC MRI (Table 1) and investigated their effects on the accuracy of the two imaging techniques.

We also performed 2D and 3D cine PC MRI using prospective ECG gating (Table 1) for the CCAs of two healthy volunteers, from whom we got informed consent. The center of the imaging slices or slab were placed 2cm below the apex of the carotid bifurcation as determined by MR angiography [3].

We calculated temporal averaged spatial mean and maximum velocities using 2D and 3D cine PC MR data set with the aid of flow visualization and analysis software (Flova; R"Tech, Hamamatsu, Japan). In the phantom study, we compared the results of 2D and 3D cine PC MR flow measurements with the measured value of the flow meter. In the volunteer study, we evaluated accuracy of 3D cine PC MRI of four CCAs of two healthy volunteers using the results of 2D cine PC MRI as a gold standard.

Table 1. Imaging Parameters

	2D cine PC	3D cine PC
Voxel size (mm ³)	0.63*-2.5	0.67*-2.0
	×	×
	0.63*-2.5	0.67*-2.0
	×	×
	5.0	0.67*-2.0
VENC (cm/sec)	150	150
TR/TE(msec)	51.7/8.86	39.76/5.23
Bandwidth (Hz/pixel)	260	476
Flip angle (degree)	15	15
Number of phases	4, 15*-16*	16*-20*, 18-25

TR, Repetition Time ; TE, Echo Time ; VENC, Velocity Encoding; * shows a parameter used for healthy volunteers.

Results

In the CCA phantom study, mean velocity based on measured value provided by the Coriolis flowmeter was 29.82 cm/sec, and the theoretical value of maximum velocity calculated by the Hagen-Poiseuille law [4] was 59.64 cm/sec; these values were considered to be the reference standard. Spatial resolution had relatively little effect on the accuracy of 2D and 3D cine PC MRI (Fig. 1). When we set the spatial resolution to around 0.65 mm (approximately 10% of the inside diameter), the measured maximum velocity approached the reference standard (Fig. 2). Errors of 2D and 3D cine PC MRI were 6.2% and 5.4% respectively and errors of mean velocities were 0.5% and 1.8% respectively.

In the healthy volunteer study, errors of temporal averaged spatial mean velocity and maximum velocity of 3D cine PC MRI were 8.8% and 8.1% respectively using the results of 2D cine PC MRI as a gold standard. In addition, temporal velocity changes during cardiac cycle obtained by 3D cine PC MRI were similar to those of 2D cine PC MRI (Fig. 3, 4).

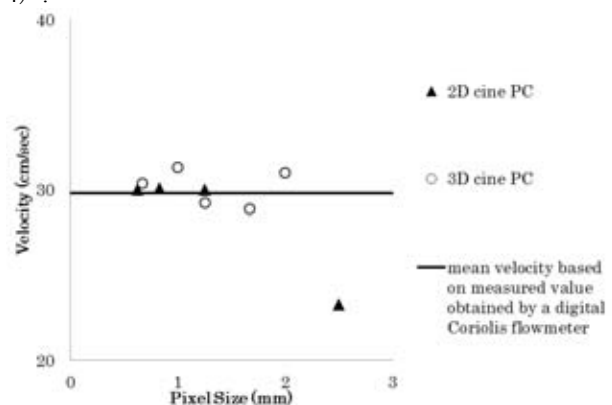


Fig. 1. Mean velocities in a 6mm inner diameter tube obtained by 2D and 3D cine PC MRI with different spatial resolution

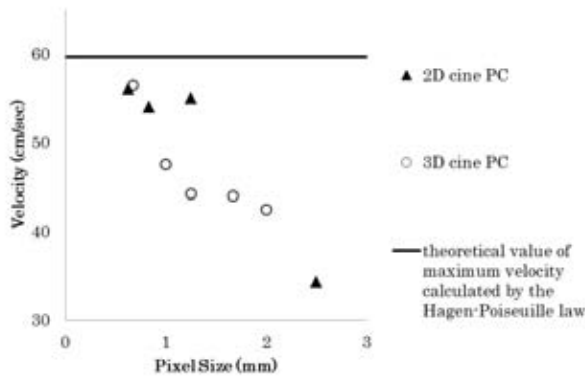


Fig. 2. Maximum velocities in a 6mm inner diameter tube obtained by 2D and 3D cine PC MRI with different spatial resolutions

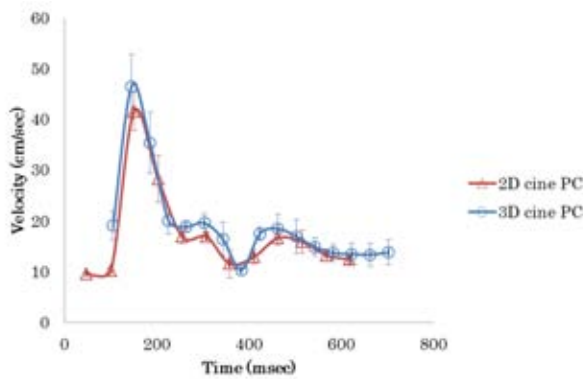


Fig. 3. Temporal changes of spatial mean velocities during cardiac cycle of the cross section 2cm below the apex of the carotid bifurcation for four common carotid arteries of two healthy volunteers obtained by 2D and 3D cine PC MRI. Error bars express standard deviations.

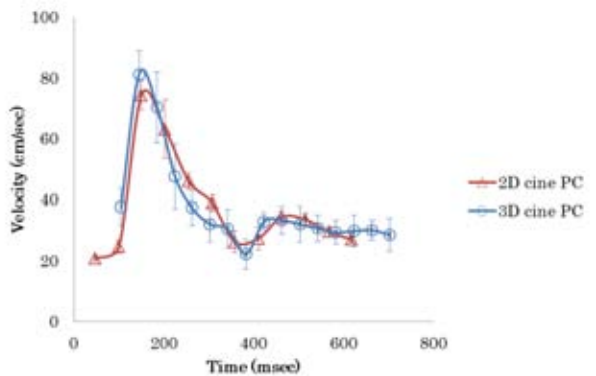


Fig. 4. Temporal changes of spatial maximum velocities during cardiac cycle of the cross section 2cm below the apex of the carotid bifurcation for four common carotid arteries of two healthy volunteers obtained by 2D and 3D cine PC MRI. Error bars express standard deviations.

Discussion

In this study, we investigated the optimal spatial resolutions of cine PC MRI for the CCA phantom, and performed and compared those two imaging techniques for CCAs of healthy volunteers.

Spatial resolution had little effect on the mean velocities in the phantom study. The mean velocity in a small tube (3 mm inner diameter) is expected to be lower than that in a large

vessel, because the vessel boundary voxels contain both the signal from vessel lumen and from the surrounding tissue, resulting in a partial volume effect [5]. It was thought that the influence of partial volume effect was relatively small in our study because the inside diameter of our phantom was 6mm.

Our phantom showed laminar flow with the largest velocity at the center of the tube. The velocity progressively decreased nearer to the wall. Maximum velocities at the center obtained by 2D and 3D cine PC MRI with high spatial resolutions approached the reference standards. A large voxel at the center of the tube was thought to include surrounding lower velocities and showed lower velocities because of partial volume effect due to low spatial resolutions.

In the volunteer study, 3D cine PC MRI temporal averaged spatial mean and maximum velocity were accurate. Temporal velocity changes during cardiac cycle obtained by this imaging technique were similar to those of 2D cine PC MRI.

Conclusions

In our study, temporal averaged spatial mean and maximum velocities of 3D cine PC MRI with a spatial resolution of around 0.65 mm were within 10% of the reference standards and temporal velocity changes during cardiac cycle obtained by this imaging technique were similar to those of 2D cine PC MRI. Our 3D cine PC MRI technique may be a viable diagnostic tool for carotid arterial disease.

References

- [1] Malek AM, Alper SL, Izumo S. Hemodynamic shear stress and its role in atherosclerosis. *JAMA*. 1999;282(21):2035-42.
- [2] Markl M, Chan FP, Alley MT, Wedding KL, Draney MT, Elkins CJ, Parker DW, Wicker R, Taylor CA, Herfkens RJ, Pelc NJ. Time-resolved three-dimensional phase-contrast MRI. *J Magn Reson Imaging*. 2003;17(4):499-506.
- [3] Sui B, Gao P, Lin Y, Gao B, Liu L, An J. Assessment of wall shear stress in the common carotid artery of healthy subjects using 3.0-tesla magnetic resonance. *Acta Radiol*. 2008;49(4):442-9.
- [4] Liu, H.-C. and Fried, J. R., Breakthrough of lysozyme through an affinity membrane of cellulose-cibacron blue. *AIChE Journal*. 1994; 40(1):40-9.
- [5] Hofman MB, Visser FC, van Rossum AC, Vink QM, Sprenger M, Westerhof N. In vivo validation of magnetic resonance blood volume flow measurements with limited spatial resolution in small vessels. *Magn Reson Med*. 1995;33(6):778-84.
- [6] Sui B, Gao P, Lin Y, Gao B, Liu L, An J. Blood flow pattern and wall shear stress in the internal carotid arteries of healthy subjects. *Acta Radiol*. 2008;49(7):806-14.
- [7] Stalder AF, Russe MF, Frydrychowicz A, Bock J, Hennig J, Markl M. Quantitative 2D and 3D phase contrast MRI: optimized analysis of blood flow and vessel wall parameters. *Magn Reson Med*. 2008;60(5):1218-31.

Author address

E-Mail: tozawa.ikki@e.mbox.nagoya-u.ac.jp

A HIGH RESOLUTION SPECT SYSTEM WITH A PHOTON COUNTING DETECTOR: MONTE CARLO SIMULATION STUDIES

Y. J. Lee¹⁾, H. J. Ryu¹⁾, S. J. Park¹⁾, D. H. Kim¹⁾, Y. S. Kim¹⁾, H. J. Kim¹⁾

1) Department of Radiological Science and Research Institute of Health Science, Yonsei University, Wonju, Korea

Introduction

Recently, new semiconductor materials such as cadmium telluride (CdTe) (density = 5.85 g/cm³) and cadmium zinc telluride (CZT) (density = 5.76 g/cm³) have become commercially available and are considered as the most promising semiconductor material for clinical imaging systems [1-2]. Especially, the signal from photons was collected individually for each pixel, and thus the intrinsic resolution of the detector is almost the same as the size of a pixel [3-7]. However a disadvantage of this detector was a loss in sensitivity due to the small pixel on the detector. By using the pixelated parallel-hole collimator, we may be able to improve the sensitivity and the spatial resolution. In this study, we simulated the SPECT system using the photon counting detector based on CdTe and CZT, and evaluated the performance of these systems.

The purpose of this paper was to evaluate high resolution SPECT system with semiconductor detector, which had very small pixels such as 0.35 × 0.35 mm², using pixelated parallel-hole collimator. For that purpose, we evaluated the sensitivity, the spatial resolution and the contrast resolution with Geant4 Application for Tomographic Emission (GATE) simulation.

Materials and Methods

Simulation set-up: To evaluate the image performance of our proposed system we performed simulations with GATE version 6 in this study. The proposed system used the CdTe and CZT detector with small pixel. The size of pixel was 0.35 × 0.35 mm² such as PID 350 CdTe detector (Ajat Oy Ltd., Finland). Also it consists of 1 mm thickness 44.8 × 44.8 mm² detector size and 128 × 128 pixel arrays. In data acquisition, the number of views was 90 over 360°, and the data acquisition time was 10 second/view. Image reconstruction was carried out with the filtered back-projection (FBP) method. However, for clarity and to ensure acceptable image quality, charge sharing was not simulated. We designed pixelated parallel-hole collimator, which has the same hole size to the pixel size. The parallel-hole collimator efficiency ($\epsilon_{\text{parallel-hole}}$) and resolution ($R_{\text{parallel-hole}}$) are the extrinsic parameters for the nuclear medicine detector and influence image performance. Equations for $\epsilon_{\text{parallel-hole}}$ and $R_{\text{parallel-hole}}$ of a parallel-hole collimator are given as follows [8]:

$$\epsilon_{\text{parallel-hole}} = \frac{1}{4\pi} \left(\frac{d}{l_{\text{effective}}} \right)^2 \frac{d^2}{(d+t)^2} \quad (1)$$

$$R_{\text{parallel-hole}} = d \frac{l_{\text{effective}} + b}{l_{\text{effective}}} \quad (2)$$

The shape of the collimator hole was square, and the size of the hole was 0.3 × 0.3 mm². The thickness of the septum was 0.05 mm and septal height was 20 mm (Figure 1).

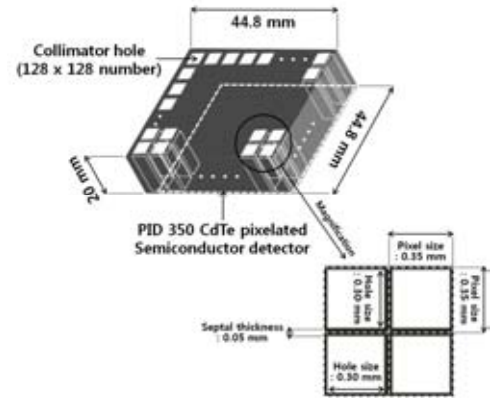


Figure 1. Schematic diagrams of the pixelated parallel-hole collimator

Evaluation of performance: In evaluating the performance of this system, we estimated both sensitivity and spatial resolution. We measured a ^{99m}Tc point source with an activity of 1 MBq (placed in air) using a scan time of 900 seconds. The distances of the point source from the collimator were 2, 4, 6, 8 and 10 cm. For the measurement of the contrast resolution, the hot-rod phantom was designed using GATE simulation (Figure 2). The phantom was filled with water and consisted of six areas with different diameters from 0.5 to 2.1 mm. The thickness of the phantom was 10 mm. In order to evaluate the improvement of the contrast resolution, we defined as follows:

$$\text{Contrast resolution} = \frac{m_p - m_v}{m_p} \times 100 (\%) \quad (3)$$

where m_p is the mean value of four peaks of a profile, and m_v is the mean value of three valleys of a profile.

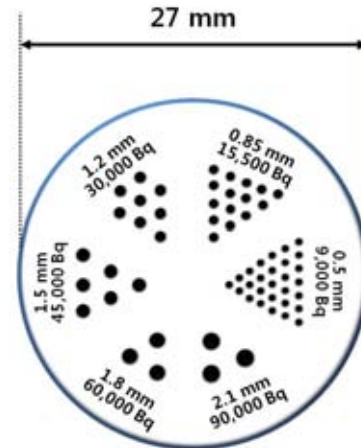


Figure 2. Hot-rod phantom diagram for evaluating the contrast resolution and overall image performance.

Results

The obtained sensitivity and spatial resolution were shown in Table 1 and 2, respectively.

Table 1 Measured the sensitivity (counts/sec/kBq) based on CdTe and CZT detector

Source to collimator distance (cm)	Sensitivity (counts/sec/kBq)	
	CdTe detector	CZT detector
2	0.00460	0.00443
4	0.00454	0.00445
6	0.00458	0.00442
8	0.00458	0.00446
10	0.00454	0.00443

Table 2 Measured the spatial resolution (mm, FWHM) based on CdTe and CZT detector

Source to collimator distance (cm)	Spatial resolution (mm, FWHM)	
	CdTe detector	CZT detector
2	0.73	0.69
4	1.01	0.98
6	1.30	1.25
8	1.55	1.54
10	1.88	1.85

Figure 3 and 4 show reconstructed images of the hot-rod phantom using CdTe and CZT detector, respectively. The results showed that the contrast resolution of CdTe and CZT detector was 90.7% and 90.3%, respectively. The results reflected the improvement of the sensitivity and the spatial resolution.

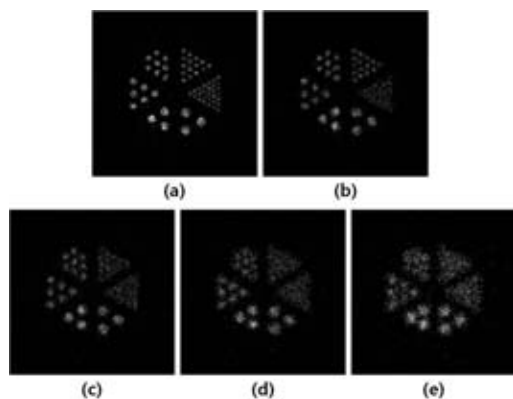


Figure 3. Reconstructed hot-rod phantom images using the CdTe detector : source to collimator distance (a) 2 cm, (b) 4 cm, (c) 6 cm, (d) 8 cm, and (e) 10 cm.

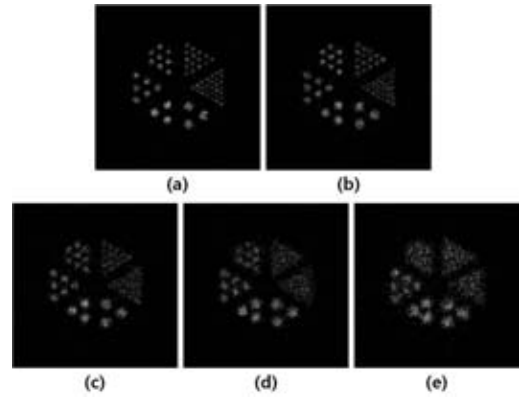


Figure 4. Reconstructed hot-rod phantom images using the CZT detector : source to collimator distance (a) 2 cm, (b) 4 cm, (c) 6 cm, (d) 8 cm, and (e) 10 cm.

Discussion

We simulated a high resolution SPECT system with a CdTe and CZT detector and pixelated parallel-hole collimator. If we apply these detectors to a pixelated parallel-hole collimator, we can acquire excellent spatial resolution since the intrinsic resolution was equal to the pixel size. In these reconstructed images, we could resolve 0.85 mm diameter when hot-rod phantom located at 2 cm from the collimator. This spatial resolution is similar to the spatial resolution of the pinhole collimator. Also the results of simulations showed that SPECT images measured with a CdTe and CZT detector had high contrast resolution and superb sensitivity in small pixel condition.

Conclusions

In conclusion, our results demonstrated that we established the high resolution SPECT system with the pixelated parallel-hole collimator.

References

- [1] Verger L, Gentet M C, Gerfault L et al. Performance and Perspectives of a CdZnTe-Based Gamma Camera for Medical Imaging. *IEEE Trans Nucl Sci.* 2004;51(6):3111-3117.
- [2] Fritz S G, Shikhaliev P M. CZT detectors used in different irradiation geometries: Simulations and experimental results. *Med Phys.* 2009;36(4):1098-1108.
- [3] Takahashi T, Watanabe S. Recent Progress in CdTe and CdZnTe detector. *IEEE Trans Nucl Sci.* 2001;48(4):950-959.
- [4] Scheiber C, Giakos G C. Medical applications of CdTe and CdZnTe detectors. *Nucl Instr Methods Phys Res A.* 2001;458:12-25.
- [5] Wen L, Yanfeng D, Brian D et al. Impact of Temperature Variation on the Energy Resolution of 3D Position Sensitive CZT Gamma-Ray Spectrometers. *IEEE Nucl Sci Con Rec.* 2007;N27-6:1809-1815.
- [6] Ogawa K, Ohumura N, Iida H et al. Development of an ultra-high resolution SPECT system with a CdTe semiconductor detector. *Ann Nucl Med.* 2009;23:763-770.
- [7] Ogawa K, Muraishi M. Feasibility Study on an Ultra-High-Resolution SPECT With CdTe Detectors. *IEEE Trans Nucl Sci.* 2010;57(1):17-24.
- [8] Wiczorek H, Goedicke A. Analytical Model for SPECT Detector Concepts. *IEEE Trans Nucl Sci.* 2006;53(3):1102-1112.

Author address

E-Mail: gloriousguy@yonsei.ac.kr